ELSEVIER

J. Non-Newtonian Fluid Mech. 138 (2006) 111–133

Journal of Non-Newtonian Fluid Mechanics

www.elsevier.com/locate/jnnfm

Time-dependent simulations of non-axisymmetric patterns in Taylor–Couette flow of dilute polymer solutions

D.G. Thomas [1], U.A. Al-Mubaiyedh [2], R. Sureshkumar *, B. Khomami

Department of Chemical Engineering and the Center for Materials Innovation, Washington University, St. Louis, MO 63130, USA

Received 25 July 2005; received in revised form 24 March 2006; accepted 10 April 2006

Abstract

Nonlinear dynamics that ensue after the inception of viscoelastic flow instabilities in homogeneous, curvilinear shear flows remain largely unexplored. In this work, we have developed an efficient, operator splitting influence matrix spectral (OSIMS) algorithm for the simulation of three-dimensional and transient viscoelastic flows. The OSIMS algorithm is applied to explore, for the first time, the post-critical dynamics of viscoelastic Taylor–Couette flow of dilute polymeric solutions utilizing the Oldroyd-B constitutive equation. Linear stability theory predicts that the flow is unstable to non-axisymmetric and time-dependent disturbances with critical conditions depending on the flow elasticity, E, defined as the ratio of the characteristic time scales of fluid relaxation to viscous diffusion. Two types of secondary flow patterns emerge near the bifurcation point, namely, ribbons and spirals. We have demonstrated via time-dependent simulations for narrow and moderate gap widths, ribbon-like patterns are generally stable at and above the linear stability threshold for $0.05 \leq E \leq 0.15$. For an inner to outer cylinder radius ratio of 0.8, the bifurcation to ribbons at $E = 0.1$ and 0.125 occurs through a subcritical transition while the transition is supercritical at smaller E values.

Keywords: Stability; Non-axisymmetric; Viscoelastic; Taylor–Couette; Influence matrix; Spectral; Bifurcation; Artificial diffusivity; Elastic turbulence

1. Introduction

The addition of high molecular weight polymers to a Newtonian flow can qualitatively alter the sequence of flow transitions as well as the critical points. Depending on the flow elasticity, characterized by the ratio of the time scale of fluid relaxation to that of viscous diffusion, and inertia, such flow transitions can lead to turbulent states whose time-averaged properties (e.g. velocity profile, drag) and (energy) spectral characteristics are dramatically different from those in the Newtonian case. In fact, it has been shown experimentally that viscoelastic flow transitions in curvilinear shear flows could result in the establishment of turbulent flow states even when the Reynolds number, Re (ratio of inertial to viscous forces) is vanishingly small [1]. This phenomenon, referred to as “elastic turbulence”, has eluded explanation based on first principle modeling/simulations. To date, the literature on the direct numerical simulation (DNS) of three-dimensional (3D) and time-dependent viscoelastic flows is limited to homogeneous shear [2] and pressure-driven channel [3,4] flows focusing primarily on the study of polymer-induced turbulent drag reduction. In this paper, we report the *first* successful simulation of 3D, time-dependent flow patterns in a viscoelastic, curvilinear shear flow.

For several decades, unidirectional shear flows with (primarily) curved streamlines of simple (Newtonian) and complex (e.g. polymeric liquids) fluids have served as classical paradigms for the investigation of hydrodynamic instabilities and pattern formation [5]. Prominent among the paradigms used for curvilinear flows is the Taylor–Couette flow in which a fluid confined between two long concentric cylinders is sheared by their relative rotation. Taylor [6], in a landmark paper in 1923, showed both theoretically as well as experimentally that the primary (base) azimuthal shear flow of a Newtonian fluid in a Taylor–Couette cell with the inner cylinder rotating and the outer stationary, becomes unstable to *axisymmetric* disturbances when $Re\sqrt{d/R_1} \approx 41$ where d is the radial gap width and R_1 is the inner cylinder radius. The instability manifests in the form of *steady* toroidal vortex cells (Taylor vortices) in the axial direction which replace the circular, base Couette flow. Theoretically, the stability threshold is determined based on a normal mode pertur-

---

* Corresponding author.
E-mail addresses: suresh@che.wustl.edu (R. Sureshkumar), bam@che.wustl.edu (B. Khomami).

[1] Present address: Department of Biomedical Engineering Washington University, St. Louis, MO 63130, USA.

[2] Present address: Department of Chemical Engineering, King Fahd University of Petroleum and Minerals, Dahran, Saudi Arabia.

0377-0257/$ – see front matter © 2006 Elsevier B.V. All rights reserved.
doi:10.1016/j.jnnfm.2006.04.013

bation analysis in which infinitesimally small disturbances are superimposed onto the primary base flow solution. Substitution of the normal mode expansion in the governing system of equations and the boundary conditions leads to a complex differential eigenvalue problem. The least negative eigenvalue determines the growth/decay rate of the perturbations. Based on several experimental and theoretical studies, a series of flow transitions that occur starting from the base Couette flow to fully turbulent flow are well documented for the Newtonian Taylor–Couette flow for different rotational speed ratios of the cylinders [7–17].

Due to the interplay between elastic and viscous/inertial forces, the instability characteristics of and flow transitions in viscoelastic curvilinear flows [18] could differ qualitatively from their Newtonian counterparts. In particular, viscoelastic shear flows with curved streamlines are prone to instabilities due to the development of hoop or normal stresses even in the absence of inertia [19–25]. Experimental studies [20–22,24–29] and linear stability analysis (LSA) [19,30] have shown that under isothermal conditions, the base circular Couette flow becomes unstable as the Deborah number (De), defined as the ratio of polymer relaxation time to the flow time scale, exceeds a critical value. For the Oldroyd-B constitutive model, LSA predicts that in the limit of $Re \to 0$, $De\sqrt{d/R_1}$ ranges between 6 and 8 depending on the ratio of solvent to total (i.e., solvent + polymer) viscosity at the critical point.

Linear stability theory based on *axisymmetric* modes predicts the existence of two possible time-periodic flow structures at the onset of instability: a standing wave characterized by radially propagating vortices and a traveling wave characterized by upward/downward axially propagating vortices. From bifurcation theory in presence of symmetries [12,31,32], it can be shown that if at least one of the bifurcations is subcritical, both of them are unstable and if both bifurcations are supercritical, then only one of the two patterns is stable. In order to compute the finite amplitude states, time integration of the governing equations can be employed. The axisymmetric and purely elastic time-dependent Taylor–Couette flow was simulated successfully using a finite-element algorithm by Northey et al. [33]. Their results showed a flow transition leading to standing waves which are in agreement with the predictions of the spectral simulations by Avgousti et al. [34] who showed that the standing wave was the stable pattern for high values of elasticity number, $E \equiv De/Re$. The traveling wave was only presumed to be stable for intermediate values of E because the simulations broke down before reaching a stable limit cycle when the standing wave was chosen as the initial solution. Kupferman [35] adopted an efficient and simple scheme based on second order central difference method to simulate the axisymmetric viscoelastic states in the inertio–elastic regime in a flow domain with at least eight wavelengths in the axial direction. His results confirmed the findings of Avgousti et al. [34].

Linear stability analysis with *non-axisymmetric* disturbances later revealed that depending on the gap width and E, such perturbations can be responsible for the primary flow instability in viscoelastic Taylor–Couette flow [28,36–38]. For instance, for the Oldroyd-B fluid model, Avgousti and Beris [36] showed that flow transitions from the circular Couette flow to non-axisymmetric and time-dependent secondary states could occur for $E \geq 0.01$. In contrast to these predictions, based on flow visualization techniques and digital particle imaging velocimetry (DPIV) measurements, Baumert and Muller [26,27] observed that the primary azimuthal flow undergoes transition to steady and axisymmetric toroidal vortices upon the inception of flow instability for purely elastic flows ($E \to \infty$). The critical onset value of Deborah number was an order of magnitude lower than that in the previous experiments [20] and that predicted by the linear stability analysis [36]. These qualitative and quantitative differences between theoretical predictions [20,36] and experimental observations [20] as well as between experiments [20,26,27] performed using different test fluids in the purely elastic Taylor–Couette flows were later resolved by the discovery of a new mode of instability, namely, the thermoelastic instability [39–41] via a non-isothermal linear stability analysis. Specifically, the thermal effects are caused by a combination of viscous heating and thermal sensitivity of the fluid. Based on a thermodynamically consistent formulation of the Oldroyd-B constitutive model, Al-Mubaiyedh et al. [39–41] predicted that, in presence of viscous heating, an axisymmetric and stationary mode with O(1) critical Deborah number is responsible for the primary instability for the purely elastic flow, which is in excellent agreement with experimental observations [26,27]. This new mode arises due to the convection of base state temperature gradients by the perturbation velocity and is dependent on the amount of viscous heating and the gap temperature gradient [39]. Nonlinear analysis shows that the stationary mode "ripens" over the time scale of thermal diffusion [41]. The bifurcation to the stationary axisymmetric mode is supercritical [41]. The interested reader may refer to [26,27,39–44] for a complete overview of thermoelastic instabilities in Taylor–Couette flow.

Thermal effects due to viscous heating become important when the ratio Γ of the polymer relaxation time, λ, to the thermal diffusion time scale, d^2/α_t, where α_t is the thermal diffusivity, is much smaller than 1. If $\Gamma \gg 1$, then one recovers the isothermal system for which LSA clearly shows that the most dangerous perturbations are non-axisymmetric and time-dependent [41]. The isothermal scenario is applicable to aqueous dilute solutions whose viscosity is significantly lower and heat capacity is significantly higher as compared to those of organic solutions such as Boger fluids. In addition, even in presence of viscous heating, higher order flow transitions could result in non-axisymmetric states if the shear rate is increased beyond a critical value [27]. Therefore, time-dependent simulation of 3D, transient flow is necessary to study nonlinear dynamics of both isothermal and non-isothermal flows.

The bifurcation to the non-axisymmetric and time-dependent secondary flow, that occurs for $\Gamma \gg 1$, has been shown to be degenerate based on the spatio-temporal symmetries of the base flow [31]. Two secondary flow patterns have been identified to emerge at the critical point – axially traveling spirals and azimuthally rotating ribbons. Based on a local nonlinear analysis [32], Renardy et al. [37] and Sureshkumar et al. [38] predicted, for narrow gaps and sufficiently large (O(1)) values of elasticity, at least one of the two non-axisymmetric families (ribbons or spirals) bifurcates subcritically, indicating that neither of the two families is stable. For a relatively wide gap width [38], the bifurcations for both spirals and ribbons are supercritical and the ribbons were shown to be the stable pattern based on a Ginzburg–Landau analysis. However, local nonlinear analysis cannot be expected to predict the flow patterns for De values appreciably greater than the critical one. This further motivates the need for a global nonlinear analysis via time-dependent simulation of the 3D, time-dependent flow to identify the pattern selection in the post-critical regime.

Recently, Groisman and Steinberg [45] performed flow visualization experiments in which, the solution elasticity was systematically varied up to three orders of magnitude to span the inertial ($E = 0$) to purely elastic ($E \gg 1$) flow regimes and investigated the effect of E. For an inner to outer cylinder radius ratio (R_1/R_2) of 0.708 and solvent to total solution viscosity ratio (β) of 0.926, two new oscillatory flow patterns were shown to exist—disordered oscillations (DO) as a result of fluid elasticity and rotating standing waves (RSW) as a result of inertial instability modified by elasticity. At a particular value of the elasticity number known as the co-dimension two point (ct-point) [46], the Couette flow becomes simultaneously unstable to both Taylor-vortex flow (TVF) and oscillatory modes. The RSW occurred as a result of the second bifurcation after the TVF. At elasticities higher than ct-point, a subcritical bifurcation from the Couette flow results in the formation of DOs. When the inner-cylinder rotation rate was reduced, the DOs decayed first to separated oscillatory strips with a central core followed by solitary vortex pairs or “diwhirls” in experiments with $\beta = 0.55$ and gap ratio of 0.829 [47,48]. The diwhirls appeared as randomly spaced axisymmetric dark rings and they decayed further to the Couette flow at a rotation velocity 45% of that at the DO onset [45,47–51].

In order to explore the diverse and complex pattern selection mechanisms in viscoelastic flows, faithful and robust simulation tools that can capture non-axisymmetric and the time-dependent states are necessary. Unlike Newtonian fluids where the stress depends on the local, instantaneous rate of deformation, the stress in polymeric liquids depends on the deformation history, typically described by a constitutive equation (C.E.). Hence, viscoelastic flow simulations require the self-consistent solution of the continuity and momentum equations in conjunction with a C.E. that describes the evolution of the viscoelastic tensor [19,52]. The C.E. introduces six additional variables for the stress that need to be computed along with the (three) velocity and (one) pressure variables in 3D transient viscoelastic flow problems. As the amplitude of the disturbance is increased, nonlinear interactions between eigenmodes become progressively stronger, hence, finer mesh resolution is required to capture the resulting spatial structures. This inevitably leads to solving a large number of equations ($(3 + 1 + 6) \times N^3$) which require prohibitively large storage space and computational time for the direct solution of the time-dependent problem. Moreover, the mixed (elliptic–hyperbolic) nature of the system of equations imposes stringent numerical stability limitations on the time step and mesh discretization [53]. In addition, the evolutionary character of the stress constitutive equation can be lost due to the loss of positive definiteness of the numerical approximation of the stress conformation tensor especially in highly elastic flow regimes, resulting in Hadamard instabilities [52,53], although new formulations that preserve the positive definiteness have been recently proposed to alleviate this problem [2,54–56].

In this study, we have implemented an operator-splitting, influence matrix spectral (OSIMS) algorithm to simulate 3D and time-dependent viscoelastic Taylor–Couette flow. The polymeric fluid is modeled using the Oldroyd-B constitutive equation [18] which qualitatively describes the shear rheology of dilute, non-shear thinning polymer solutions. This paper is organized as follows. The viscoelastic Taylor–Couette problem is formulated in Section 2, followed by a description of the OSIMS algorithm in Section 3. The validation and performance details of the OSIMS code as compared to a fully implicit method, and parallel implementation for 3D transient viscoelastic flow computations are presented in Section 4. Subsequently, linear and nonlinear stability analyses are discussed in Section 5. Section 6 deals with the implementation of the OSIMS algorithm with a global artificial diffusivity to stabilize the time-integration of the C.E. We present our conclusions in Section 7.

2. Problem formulation

Consider a Taylor–Couette system with rotating inner and stationary outer cylinder with radius R_1 and R_2, respectively. Let the angular velocity of the inner cylinder be denoted by Ω_1. Let η_T, ρ and λ denote the total solution viscosity, fluid density and average relaxation time of the polymer solution, respectively. The total solution viscosity η_T is the sum of the solvent (η_S) and polymeric (η_P) contributions, i.e., $\eta_\mathrm{T} = \eta_\mathrm{S} + \eta_\mathrm{P}$. We choose gap width $d \equiv R_2 - R_1$, $d/(R_1\Omega_1)$, $R_1\Omega_1$, $\rho(R_1\Omega_1)^2$ and $\eta_\mathrm{P}R_1\Omega_1/d$ as the scales for length, time, velocity, pressure and polymeric stress, respectively. Then the non-dimensional momentum equation can be written for an incompressible ($\nabla\cdot\mathbf{u} = 0$) viscoelastic fluid as

$$\frac{\partial \mathbf{u}}{\partial t} = \mathbf{u} \times \boldsymbol{\omega} - \nabla P + \frac{1}{Re}\nabla^2\mathbf{u} - E(1-\beta)\,\nabla\cdot\boldsymbol{\tau}_{(1)}, \qquad (1)$$

where $\mathbf{u}$ denotes the velocity vector with components u_r, u_θ and u_z in the r, θ and z directions of a cylindrical coordinate system with the z-axis coinciding with that of the cylinders, respectively, β is the solvent to total viscosity ratio, $\omega \equiv \nabla \times \mathbf{u}$, the Reynolds number $Re \equiv \rho R_1\Omega_1 d/\eta_\mathrm{T}$, P denotes the hydrodynamic pressure, and $\boldsymbol{\tau}_{(1)}$ denotes the upper convected derivative of polymeric stress, $\boldsymbol{\tau}$, defined as

$$\boldsymbol{\tau}_{(1)} \equiv \frac{\partial \boldsymbol{\tau}}{\partial t} + \mathbf{u}\cdot\nabla\boldsymbol{\tau} - [(\nabla\mathbf{u})^t\cdot\boldsymbol{\tau} + \boldsymbol{\tau}\cdot\nabla\mathbf{u}]. \qquad (2)$$

The Oldroyd-B constitutive model used in this work can be derived from either molecular theory for dilute polymer solutions in which the polymer molecules are modeled as non-interacting Hookean elastic dumbbells or continuum mechanics based on a generalized spring-dashpot model:

$$\boldsymbol{\tau}_{(1)} = -\frac{1}{De}[\boldsymbol{\tau} - (\nabla\mathbf{u} + (\nabla\mathbf{u})^t)], \qquad (3)$$

where the Deborah number $De \equiv \lambda R_1\Omega_1/d$.

Eqs. (1)–(3) are supplemented with the no-slip boundary condition at the cylinder walls.

3. Simulation algorithm

We have developed a CPU and memory efficient, stable time integration algorithm based on the concepts of operator splitting and influence matrix technique to enforce the divergence free velocity field on the boundary [4,15,16,34,53,57–59]. The salient features of this spectral (in space) [58], multi-step (in time) algorithm are explained below.

3.1. Spatial discretization

Spatial discretization is accomplished via the use of exponentially convergent spectral basis functions: Chebyshev polynomials in the radial (r) direction and Fourier basis functions in the axial (z) and azimuthal (θ) directions leading to

$$\mathbf{u}(t, r, z, \theta) = \sum_{l=0}^{L} \sum_{j=-J/2}^{J/2-1} \sum_{k=-K/2}^{K/2-1} \hat{\mathbf{u}}_{ljk}(t)\, T_l(r)\, \mathrm{e}^{i(2\pi\, jz/L_z + k\theta)} \tag{4}$$

where i is the imaginary unit ($i \equiv \sqrt{-1}$), L_z is the length of the computational domain along the cylinder axis, $T_l(r)$ is the Chebyshev polynomial of degree l, the complex exponentials represent the complex Fourier series for the axial and azimuthal directions truncated at $J/2$ and $K/2$, respectively, and $\hat{\mathbf{u}}_{ljk}(t)s$ are the spectral coefficients. Note that these choices for the basis functions further allow for the use of $O(N \log(N))$ fast Fourier transform (FFT) for the evaluation of spectral coefficients as well as easy evaluation of the derivatives as discussed in the context of viscoelastic turbulent channel flow simulations by Sureshkumar et al. [4]. After substitution of the spectral expansion for the flow variables in the governing equations, a Galerkin projection is implemented leading to a system of ordinary differential equations (in time) for the $10JK(L+1)$ spectral coefficients $\hat{\mathbf{u}}_{ljk}(t)$. Hence, fully implicit time-integration techniques are infeasible even for coarse meshes. Hence, we employ a multi-step, operator splitting method for the time-integration of the spectral coefficients. However, operator splitting will lead to algorithms with conditional numerical stability and will require special treatment for the satisfaction of the incompressibility constraint. Although such methods have been well-developed for Newtonian flows, robust operator-splitting (OS) algorithms for *non-axisymmetric*, viscoelastic flow simulations for large values of Re and O(10) De do not exist. Previous work in this area by us and others has developed efficient algorithms to track axisymmetric transitions [31,41,60]. However, in axisymmetric implementations the momentum and continuity equations are typically solved simultaneously, there by eliminating the need for special techniques to ensure the satisfaction of the divergence free constraint for the velocity field. The large size of the coupled ($\mathbf{u}$, P) problem makes its simultaneous solution infeasible. Hence, the momentum equation (1) is split into three parts as outlined below.

3.2. Time-integration using the OSIMS algorithm

In the OSIMS technique the velocity is updated in three steps to produce an intermediate solution (denoted by *), which will be corrected later to ensure the satisfaction of the incompressibility constraint. In the first step, the inertial and polymeric stress contributions are updated explicitly using an Adams–Bashforth (AB) second order method, i.e.:

$$\frac{\mathbf{u}^{n+1/3*} - \mathbf{u}^n}{\Delta t} = \frac{3}{2}\left(\mathbf{u} \times \omega + \frac{1-\beta}{Re}\nabla \cdot \boldsymbol{\tau}\right)^n - \frac{1}{2}\left(\mathbf{u} \times \boldsymbol{\omega} + \frac{1-\beta}{Re}\nabla \cdot \boldsymbol{\tau}\right)^{n-1}, \tag{5}$$

where Δt is the time step size. In the second and third steps, we account implicitly for the pressure and viscous contributions. Based on past literature on numerical stability of the overall time-integration procedure [15] and storage considerations, we have chosen here a first order implicit Euler method that gives:

$$\frac{\mathbf{u}^{n+2/3*} - \mathbf{u}^{n+1/3*}}{\Delta t} = -\nabla P^{n+1*} \tag{6}$$

and

$$\frac{\mathbf{u}^{n+1*} - \mathbf{u}^{n+2/3*}}{\Delta t} = \frac{\beta}{Re}\nabla^2 \mathbf{u}^{n+1*}. \tag{7}$$

Note that the pressure P^{n+1*} in Eq. (6) is still unknown. Therefore, before implementing the second step, a Poisson equation for the pressure is derived by taking the divergence of Eq. (6) and enforcing that $\mathbf{u}^{n+2/3*}$ is divergence free, i.e.:

$$\nabla^2 P^{n+1*} = \frac{\nabla \cdot \mathbf{u}^{n+1/3*}}{\Delta t}. \tag{8}$$

Eq. (8) is solved subject to homogeneous boundary conditions for the pressure. Hence, the solution needs to be corrected for the true pressure boundary conditions. Therefore, the influence matrix [57] has to be evaluated and used along with the intermediate solution to evaluate the true pressure boundary conditions. In order to evaluate the influence matrix, the following Stokes problem is solved:

$$\nabla^2 p_i = 0, \qquad p_i(r_j) = \delta_{ji}, \tag{9a}$$

$$\frac{\beta}{Re}\nabla^2 \mathbf{u}_i - \nabla p_i = \frac{\mathbf{u}_i}{\Delta t}, \qquad \mathbf{u}_i(r_j) = 0 \tag{9b}$$

where $i = 1,\ldots,N$ and N is the total number of grid points on the cylinder wall (i.e., $N = 2KJ$, see Eq. (4)). In the above equations, r_j ($j = 1, 2,\ldots, N$), represent the grid points on the cylinder walls and δ_{ji} is the Kronecker delta. By solving Eqs. 9(a) and 9(b), a total of N linearly independent solutions are constructed. The influence matrix, denoted by $\mathbf{H}$, is then evaluated from the divergence of the velocities, $\mathbf{u}_i$, at the cylinder walls as follows:

$$\mathbf{H}_{ji} = \nabla \cdot \mathbf{u}_i(r_j). \tag{10}$$

The solutions to Eqs. (9a) and (9b) and the influence matrix are evaluated and stored in a pre-processing stage. The corrected solution at the end of each time step, P^{n+1} and $\mathbf{u}^{n+1}$ can now be constructed by the following linear superposition as

$$P^{n+1} = P^{n+1*} + \sum_{i=1}^{N} \gamma_i p_i, \tag{11a}$$

$$\mathbf{u}^{n+1} = \mathbf{u}^{n+1*} + \sum_{i=1}^{N} \gamma_i \mathbf{u}_i, \tag{11b}$$

where the coefficients γ_i are chosen by solving the system of equations given by

$$\mathbf{H}_{ij}\gamma_i = -\nabla \cdot \mathbf{u}^{n+1*}(r_i). \tag{12}$$

Finally, we note that the integration of the evolution equation for the polymeric stress is performed explicitly using a second-order accurate Adams–Bashforth formula:

$$\frac{\boldsymbol{\tau}^{n+1} - \boldsymbol{\tau}^{n}}{\Delta t} = \frac{3}{2} f(\boldsymbol{\tau}^{n}, \mathbf{u}^{n}) - \frac{1}{2} f(\boldsymbol{\tau}^{n-1}, \mathbf{u}^{n-1}), \tag{13}$$

where

$$f = -\frac{1}{De}[\boldsymbol{\tau} - (\nabla\mathbf{u} + (\nabla\mathbf{u})^t)] - \mathbf{u} \cdot \nabla\boldsymbol{\tau} + [(\nabla\mathbf{u})^t \cdot \boldsymbol{\tau} + \boldsymbol{\tau} \cdot \nabla\mathbf{u}]. \tag{14}$$

The initial solutions for the time-dependent simulations are constructed by superposition of the respective eigenfunctions corresponding to the leading eigenvalue obtained from LSA onto the base flow solution.

4. OSIMS algorithm: performance, validation and parallel implementation

This section is divided into four subsections. In Section 4.1, the CPU and memory efficiency of the operator splitting algorithm based on the influence matrix method is compared to that of the fully implicit algorithm [41,60] for the case of an axisymmetric Newtonian Taylor–Couette flow. In Section 4.2, we compare our results with those obtained from the fully implicit algorithm for axisymmetric transitions [41,60] as well as selected experimental [61] and computational [17] results available in the literature. In Section 4.3 we perform comparison between OSIMS and theoretical bifurcation analysis [13] for the non-axisymmetric Newtonian flow. In Section 4.4, we present the details of the implementation of OSIMS algorithm on a parallel-computing platform.

4.1. OSIMS algorithm: performance

By simulating the axisymmetric Newtonian flow (TVF) using both OSIMS and fully implicit algorithms, the CPU time and memory requirements for each algorithm are calculated and plotted in Fig. 1 as a function of the total number of unknowns in the simulation. All simulations are performed on a DEC alpha ES40 Linux workstation with a single 833 MHz processor and 14GB of RAM. The number of unknowns is equivalent to the product of the number of partial differential equations and the total number of mesh points. In this case, it is equal to $4 \times L \times J$, where L and J represent the number of mesh points in the radial (Chebyshev) and axial (Fourier) directions, respectively. It is clear from Fig. 1 that the CPU and memory requirements of the OSIMS algorithm are several orders of magnitude lower than those of the fully implicit technique. Therefore, as expected, the OSIMS algorithm is extremely CPU and memory efficient in comparison to the fully implicit technique.

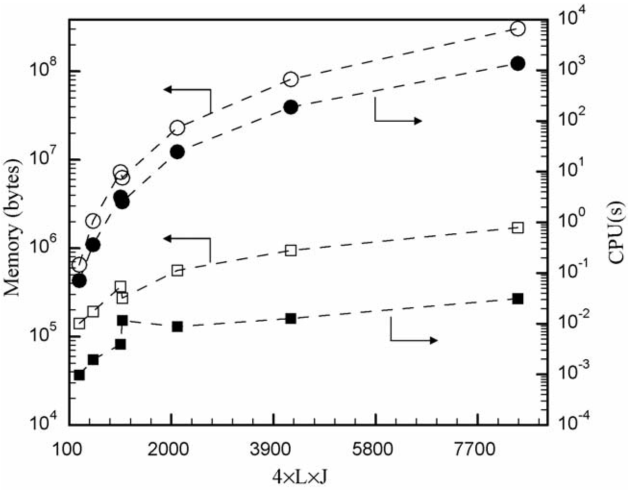

Fig. 1. Comparison (semi-log plot) of memory size and CPU time (per time step) requirements for the fully implicit method (●, ○) vs. influence matrix method (■, □) for axisymmetric Newtonian Taylor–Couette flow.

The scaling of the CPU time and memory requirements with respect to the number of mesh points in the radial and axial directions is shown in Fig. 2 for the two algorithms. For the fully implicit algorithm based on the Newton–Raphson method, the required CPU time scales as $(4 \times L \times J)^3$ while the memory size requirements are of $O(4 \times L \times J)^2$ (Fig. 2(a)). The fully implicit algorithm, when based on a modified Newton-Raphson's method in which the Jacobian matrix is updated only after every 50 time steps and after every 40 iterations within a time step, requires CPU time only of the order $\mathrm{O}(4 \times L \times J)^2$ (Fig. 2(b)). The OSIMS algorithm, on the other hand, needs only $\mathrm{O}(4 \times L^2 \times J)$ amount of CPU time and memory size (Fig. 2(c)). This is due to the linearity of the implicitly treated elliptic operators described in Section 3. Specifically, for the Poisson and Helmholtz operators, the Fourier modes in the axial direction decouple. Hence, for each of the J Fourier modes, we perform a back substitution for four $L \times L$ matrices each involving $\mathrm{O}(L^2)$ operations.

4.2. OSIMS algorithm: validation

In order to validate the accuracy of the OSIMS algorithm, its predictions are compared with the fully implicit algorithm [60] as well as experimental [61] and computational [17] results available from the literature for the axisymmetric Newtonian Taylor-vortex flow as shown in Table 1. We compute the torque at the inner cylinder for $Re > Re_c$ (critical Reynolds number) as the flow evolves from the base azimuthal flow to the Taylor vortex flow. The torque exerted by the fluid on the inner cylinder

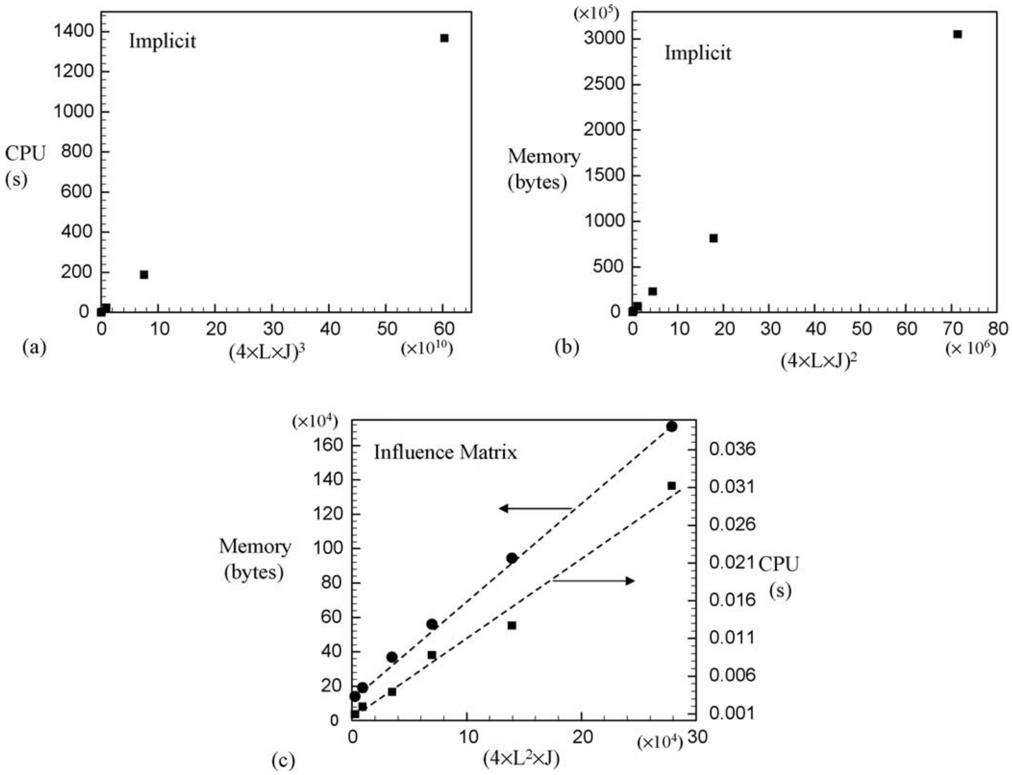

Fig. 2. Scaling of memory size and CPU time requirements with the number of points in the radial (L) and the axial (J) directions for axisymmetric Newtonian Taylor–Couette flow: (a) fully implicit method (CPU time), (b) fully implicit method (memory size) and (c) influence matrix method (memory size and CPU time).

is calculated based on the formula:

$$G = 2\pi r_1 Re\left(\frac{\mathrm{d}(r\bar{u}_\theta)}{\mathrm{d}r} - 2\bar{u}_\theta\right) \tag{15}$$

where G is the dimensionless torque (per unit length) normalized with respect to η^2/ρ and the over bar denotes an average over the axial direction. Specifically, we perform the calculations for a gap ratio of 0.95 and 0.5 at a Reynolds number equal to 195 and 78.6, respectively. The corresponding critical axial wavenumbers (α_c) made dimensionless with respect to the gap width ($\alpha = (2\pi d)/L_z$) are 3.128 and 3.161, respectively. Moser et al. [17] used pseudo-spectral methods that inherently satisfy the boundary conditions and the continuity equation. They used 11×10 points in r- and z-axes to evaluate the linear terms while 17×16 points were required to evaluate the nonlinear terms so that aliasing errors are minimized. They compared their results for torque at the inner cylinder with the experiments of Donnelly and Simon [61] for the two gap widths as shown in Table 1. The torque values predicted by Moser et al. [17] agreed with the experimentally observed values by Donnelly and Simon [61] within 3% and 0.5% for 0.95 and 0.5 gap ratios, respectively. The prediction of the fully implicit and OSIMS algorithms from the present study are also tabulated in Table 1 using $\Delta t = 0.1$ and without de-aliasing. The results obtained from both methods are in good agreement with the calculations of Moser et al. [17] as well as the experiments of Donnelly and Simon [61].

4.3. Application of OSIMS algorithm to non-axisymmetric Newtonian flows

In the Newtonian Taylor–Couette flow, the primary transition to axisymmetric and stationary toroidal vortex flow occurs when the inner cylinder is rotating while the outer cylinder is at rest. However, when both the cylinders are rotating, non-

Table 1
Newtonian Taylor-vortex flow: comparison of calculated torque at the inner cylinder with literature values ($\Delta t = 0.1$)

Parameters	Experiments [61]	Calculation [17]	Present calaculation		
			Fully implicit	Influence matrix	$r \times z$ points
$R_1/R_2 = 0.95$	5.26×10^5	5.42×10^5	5.4186×10^5	5.4391×10^5	9×8
$\alpha_c = 3.128$			5.4184×10^5	5.4180×10^5	17×8
$Re = 195$			5.4184×10^5	5.4184×10^5	17×16
$R_1/R_2 = 0.5$	1.479×10^3	1.487×10^3	1.4848×10^3	1.4848×10^5	33×8
$\alpha_c = 3.161$			1.4988×10^3	1.4988×10^3	17×16
$Re = 78.6$			1.4846×10^3	1.4846×10^3	33×16

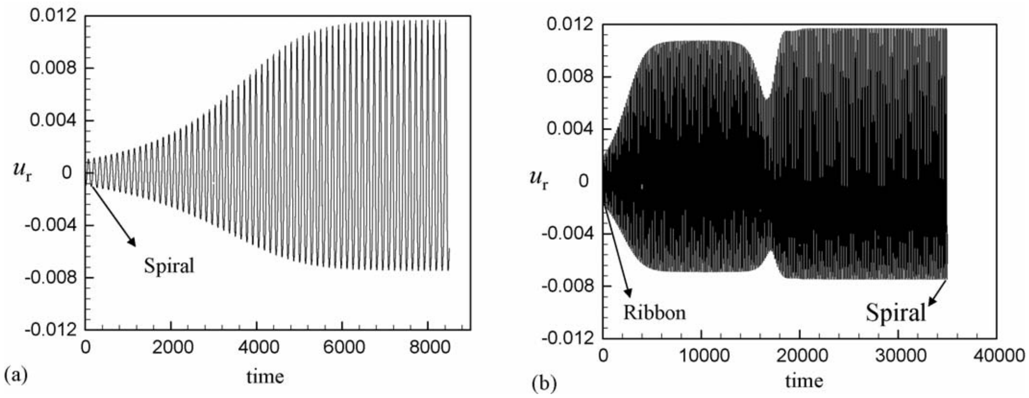

Fig. 3. Time evolution of radial velocity for Newtonian Taylor–Couette flow at the center of the computational domain ($r=(r_1+r_2)/2, \theta=\pi, z=\pi/\alpha$) for $R_1/R_2=0.883$, $\alpha=3.517$, $Re_2=-129.05$ and $Re_1=167.2$. (a) Spiral flow initial condition and (b) ribbon flow initial condition. All initial conditions are superimposed over the steady state solution.

axisymmetric and time-dependent transitions are likely to occur [7]. Andereck et al. [7] had carried out an extensive set of experiments that revealed a wide variety of flow states in the Taylor–Couette flow when the cylinders are either co-rotating or counter-rotating. Here, we present calculations for the case where the cylinders are counter-rotated. Specifically, the outer cylinder rotation rate, Ω_2, is held fixed while the inner cylinder rotation rate is varied to explore different flow states. We denote the Reynolds number based on the outer and inner cylinder radius as $Re_2 \equiv \pm\rho R_2 \Omega_2 d/\eta_T$ and $Re_1 \equiv \pm\rho R_1 \Omega_1 d/\eta_T$, respectively. The negative sign corresponds to counter rotation (clockwise direction with respect to the θ coordinate).

Golubitsky and Langford [13] had performed local nonlinear stability analysis to calculate the bifurcation diagrams at the point of bistability (0, 1) for large, moderate and small gap widths. The point of bistability (0, 1) is defined as the point at which the primary bifurcation changes from an axisymmetric ($\xi=0$) to a non-axisymmetric ($\xi=1$) branch. This occurs

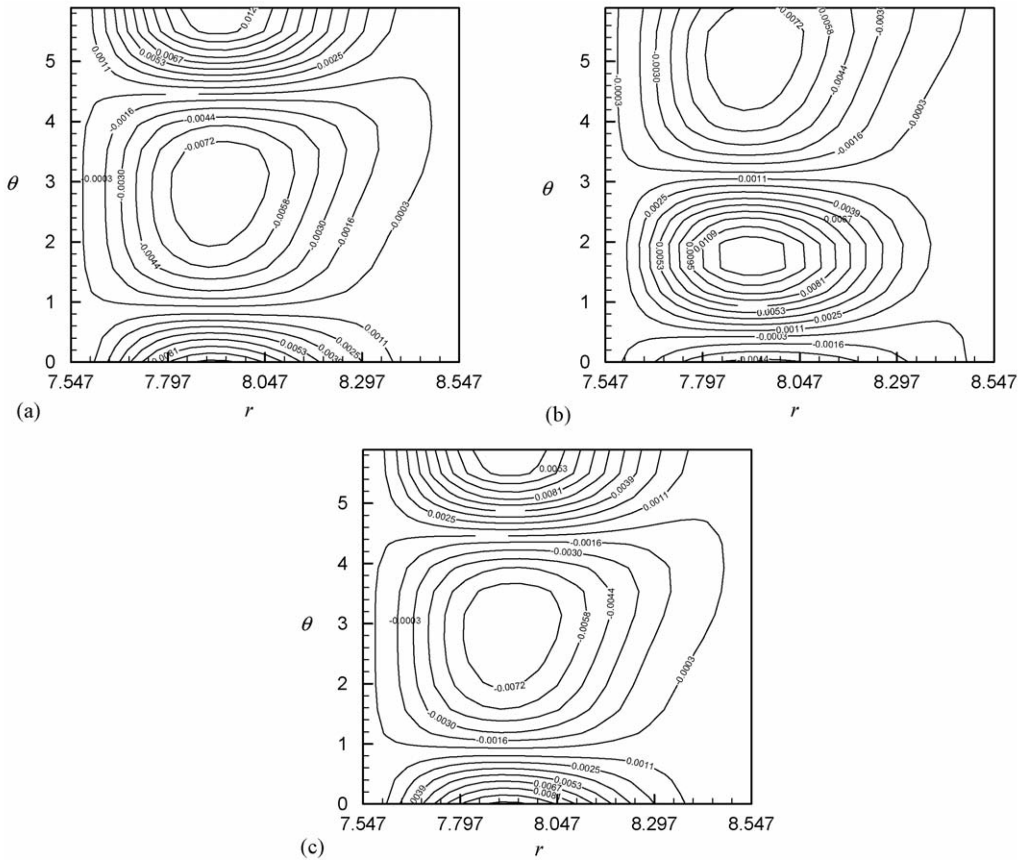

Fig. 4. Newtonian secondary flow contour plots of radial velocity (u_r) in r–θ plane ($z=\pi/\alpha$) for $R_1/R_2=0.883$, $\alpha=3.517$, $Re_2=-129.05$ and $Re_1=167.2$ corresponding to spirals of Fig. 3(a) about time = 8000 where amplitude is (a) minimum, (b) zero and (c) maximum.

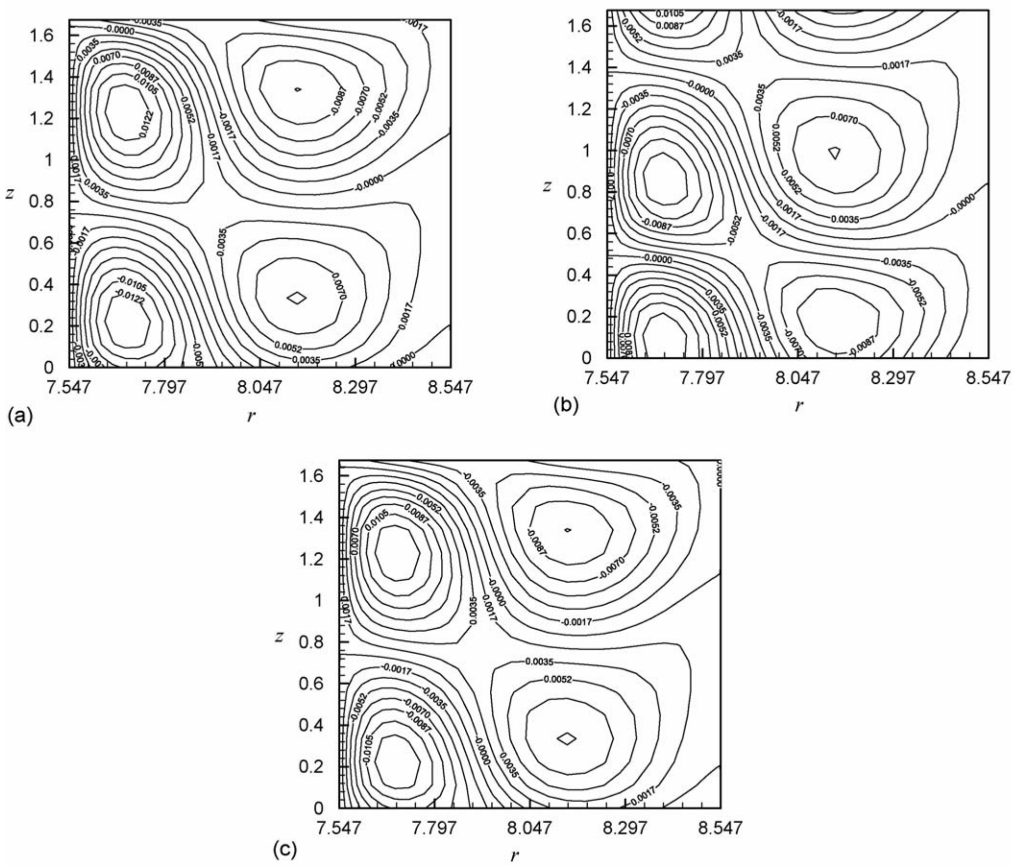

Fig. 5. Newtonian secondary flow contour plots of axial velocity (u_z) in r–z plane ($\theta = \pi$) for $R_1/R_2 = 0.883$, $\alpha = 3.517$, $Re_2 = -129.05$ and $Re_1 = 167.2$ corresponding to spirals of Fig. 3(a) about time = 8000 where amplitude is (a) minimum, (b) zero and (c) maximum.

when the $|Re_2|$ is increased above a critical value denoted by $|Re_2|_{c01}$. Similarly, increasing $|Re_2|$ further leads to bistabilities (1, 2), (2, 3) and so on. By varying Re_1 as a bifurcation parameter, Golubitsky and Langford [13] showed, that for a relatively wide gap ($R_1/R_2 = 0.736$), both the axisymmetric (for $|Re_2|$ slightly lower than $|Re_2|_{c01}$) and non-axisymmetric bifurcations (for $|Re_2|$ slightly higher than $|Re_2|_{c01}$) are supercritical. For a smaller gap $R_1/R_2 = 0.883$, the axisymmetric bifurcation is subcritical while the non-axisymmetric one remains supercritical. For a narrow gap ($R_1/R_2 = 0.95$), however, both the axisymmetric and non-axisymmetric transitions are subcritical. Using Hopf bifurcation theory in presence of symmetry, Golubitsky and Langford [13] showed that the non-axisymmetric transitions will result in either one of two possible patterns, namely, spirals and ribbons.

The OSIMS algorithm was used to perform nonlinear stability analysis using time-dependent simulations for a moderate gap ratio of 0.883 that was previously considered by Golubitsky and Langford [13] and Andereck et al. [7]. From linear stability analysis for counter-rotating cylinders, the critical conditions at the bistability point (0, 1) are $\alpha_c = 3.517$, $|Re_2|_{c01} = 128.95$ and $Re_{1c} = 166.89$. The simulations are carried out using 33 (radial) × 16 (axial) × 16 (azimuthal) with a time step size of 0.1. In Fig. 3 we present the time evolution of the radial velocity for $\alpha_c = 3.517$, $Re_2 = -129.05$ and $Re_1 = 167.2$ for both the spiral (see Fig. 3 (a)) as well as ribbon (see Fig. 3(b)) initial conditions. Specifically, the spiral patterns are characterized by an azimuthal wavenumber, $\xi = 1$ as shown in the $r - \theta$ contour plots of radial velocity in Fig. 4(a)–(c). The axial velocity is also plotted in the r–z and θ–z planes in Figs. 5 and 6, respectively, which indicate spiral structures. This is consistent with the bifurcation analysis [13] that predicts a stable spiral flow pattern for $R_1/R_2 = 0.883$. From Fig. 3(b), it is seen that the ribbon solution becomes unstable and evolves into a stable spiral, and this is elucidated by the θ–z contour plots of the axial velocity in Fig. 7 at dimensionless time $t = 10{,}000$ (Fig. 7(a)) and at $t = 22{,}000$ (Fig. 7(b)). When $Re_2 = -128.95$, the secondary flow manifests in the form of stationary Taylor vortex cells ($\xi = 0$) as shown in Fig. 8 that is also in agreement with the bifurcation analysis [13]. In Fig. 9, the amplitude of the radial velocity at the center of the computational domain is plotted against ($Re_1 - Re_{1c}$) for the inner cylinder to investigate the bifurcation characteristic of the spiral (Fig. 9(a)) and TVF (Fig. 9(b)) solutions. A bifurcation diagram is constructed by plotting the radial velocity amplitude versus $Re_1 - Re_{1c}$. The bifurcation diagrams indicate supercritical and subcritical bifurcation of the spirals and TVF, respectively. Moreover, the amplitude corresponding to the (spiral) supercritical bifurcation follows a square-root dependence on $Re_1 - Re_{1c}$ that is in agreement with bifurcation theory for supercritical bifurcation near the stability threshold.

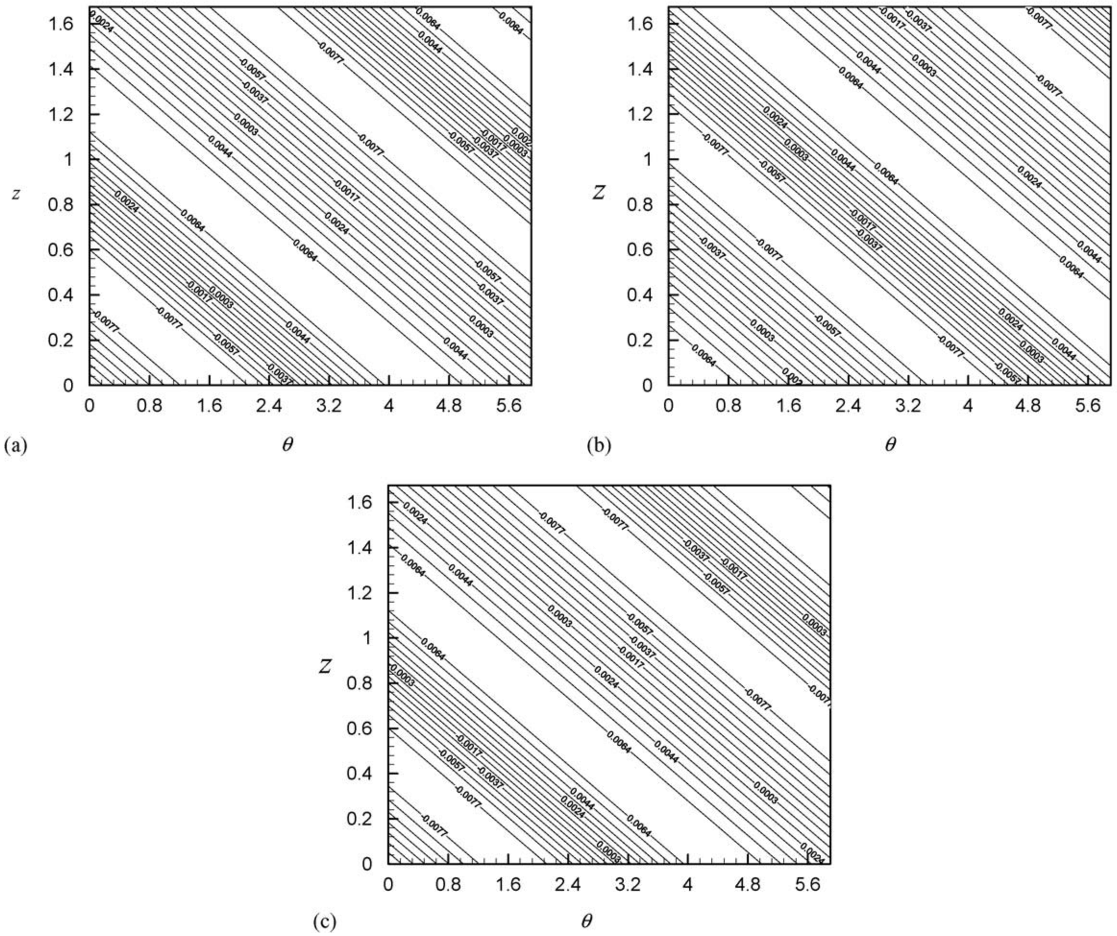

Fig. 6. Newtonian secondary flow contour plots of axial velocity (u_z) in θ–z plane ($r=(r_1+r_2)/2$) for $R_1/R_2=0.883$, $\alpha=3.517$, $Re_2=-129.05$ and $Re_1=167.2$ corresponding to spirals of Fig. 3(a) about time = 8000 where amplitude is (a) minimum, (b) zero and (c) maximum.

4.4. Parallel implementation of OSIMS algorithm

Time-dependent simulation of 3D viscoelastic flows to predict the experimentally observed flow states [1,45,47,48] requires large memory storage space and computation time. In order to perform fast and efficient simulations, we successfully implemented the OSIMS algorithm on a parallel supercomputing platform (SGI-ORIGIN 2000) at the Center for Scientific Parallel Computing (CSPC) at Washington University (St. Louis). The ORIGIN has a 64GB shared memory system

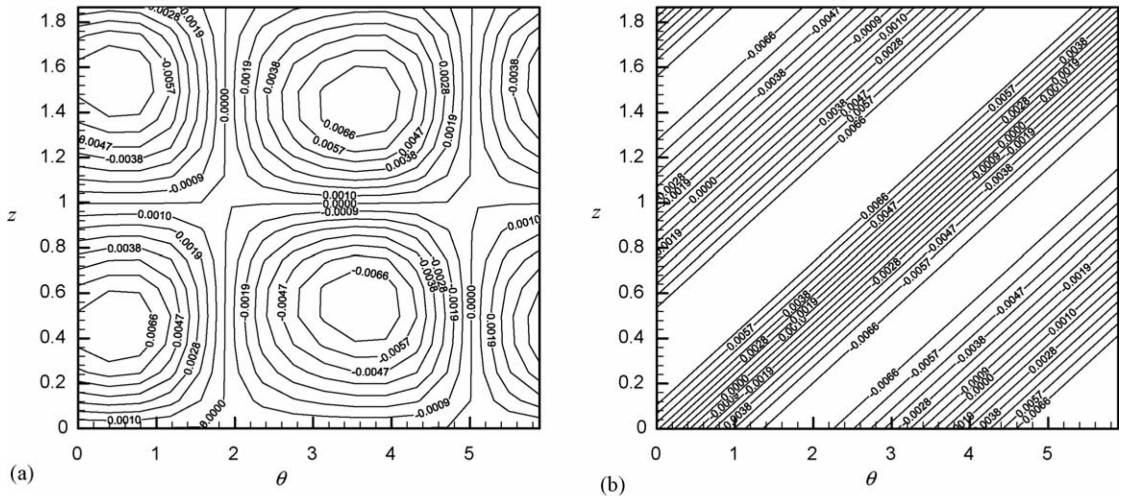

Fig. 7. Newtonian secondary flow contour plots of axial velocity (u_z) in θ–z plane ($r=(r_1+r_2)/2$) for $R_1/R_2=0.883$, $\alpha=3.517$, $Re_2=-129.05$ and $Re_1=167.2$ for the ribbon to spiral transition of Fig. 3(b). (a) Ribbon at time = 10,000 and (b) spiral at time = 22,000.

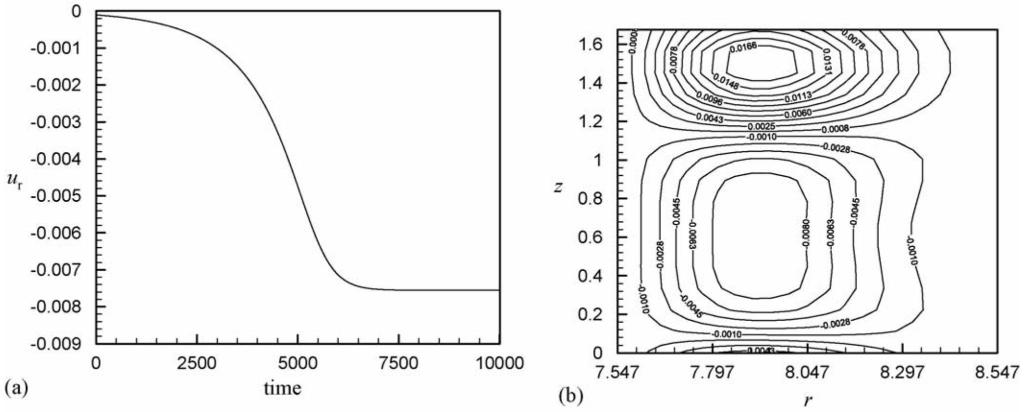

Fig. 8. Newtonian Taylor-vortex (TVF) flow. (a) Time evolution of radial velocity at the center of the computational domain ($r = (r_1 + r_2)/2$, $\theta = \pi$, $z = \pi/\alpha$) for $R_1/R_2 = 0.883$, $\alpha = 3.517$, $Re_2 = -128.85$, $Re_1 = 167.2$ and (b) final contour plot of radial velocity (u_r) in r–z plane ($\theta = \pi$).

and is equipped with 64×R12000 MIPS processors with 400 MHz clock speed per processor and 8MB L2 cache. Since, the dependent flow variables are spectrally decomposed in Fourier modes in both azimuthal (θ) and axial (z) directions, it is easier to distribute the z and θ planes among the processors/nodes. Note that in the current implementation, only the θ planes are distributed among the processors. Since the OSIMS algorithm updates the spectral coefficients, the nonlinear terms have to be computed in physical space. Hence, spectral to/from physical space transformations are required, necessitating communication between the processors. This is achieved by using MPI (Message Passing Interface) protocol.

In order to measure the performance of the parallel OSIMS algorithm, we calculate the speed-up (S(np)) and efficiency (Ef(np)) with the number of processors (np) and the total degrees of freedom. Specifically, we perform a 3D, time-dependent viscoelastic flow simulation for 1000 time steps and record the execution time (t(np)) on np number of processors for different mesh sizes as tabulated in Table 2. The speed-up of a parallel program is a measure of how fast the program runs on np (≥1) processors compared to 1 processor, i.e.:

$$S(\mathrm{np}) = \frac{t(1)}{t(\mathrm{np})}, \tag{16}$$

while the efficiency is given by

$$\mathrm{Ef}(\mathrm{np})\,(\%) = \frac{S(\mathrm{np})}{\mathrm{np}} \times 100. \tag{17}$$

An efficiency of 100% ($S(\mathrm{np}) = \mathrm{np}$) corresponds to a linear speed-up of the program with the number of processors, which is the best theoretical achievable limit although there are exceptions where super-linear speed-up can occur due to the effects of cache architecture and optimization of MPI communications on the super-computing platform. As clearly seen from Table 2, the total time required to complete the simulation reduces with increase in the number of processors for all mesh sizes studied. For example, a single processor requires about 6.5 h to run 1000 time steps for a problem size of ≈2.7 million degrees of freedom (=10 × 65 × 64 × 64), while the simulation takes only about 16 min with 32 processors (see Fig. 10(a)). For large mesh sizes, about 90–96% reduction in time is achieved with 32 processors. Overall, the speed-up of the parallel program follows sub-linearly with the number of processors as the problem size becomes larger as shown in Fig. 10(b). However, it is encouraging to note that as mesh size is increased, the efficiency and speed-up increase as well and for the largest mesh size investigated here (65 × 64 × 64), the program runs at 75% efficiency with 32 processors. This can be attributed to the fact that for

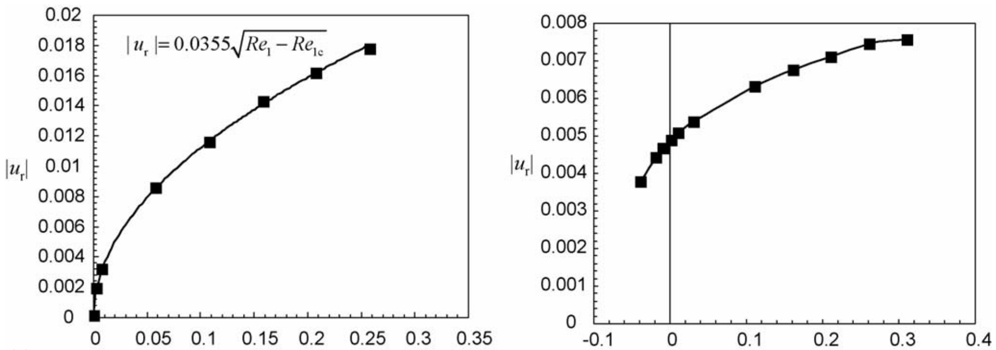

Fig. 9. Bifurcation diagram of final radial velocity (u_r) amplitude of Newtonian Taylor–Couette flow at the center of the computational domain ($r = (r_1 + r_2)/2$, $\theta = \pi$, $z = \pi/\alpha$) for $R_1/R_2 = 0.883$, $\alpha = 3.517$, $Re_{1c} = 167.2$. (a) $Re_2 = -129.05$ (spiral flow) and (b) $Re_2 = -128.85$ (TVF).

Table 2
Parallel implementation of OSIMS algorithm for 3D time-dependent viscoelastic Taylor–Couette flow: speed-up and efficiency

Mesh size ($r/z/\theta$)	No. of processors, np	Real execution time, t(np) (min)	Maximum memory required (MB)	Swap memory required (MB)	Speed-up, $S(\mathrm{np}) = t(1)/t(\mathrm{np})$	Efficiency, $\mathrm{Ef}(\mathrm{np}) = 100S(\mathrm{np})/\mathrm{np}$ (%)
33/16/16	1	7.57	16	52	1	100
	2	4.87	28	82	1.6	77.7
	4	3.12	44	139	2.4	60.7
	8	1.98	76	286	3.8	47.7
	16	1.73	140	707	4.4	27.3
33/32/32	1	33.00	34	90	1	100
	2	19.85	52	123	1.7	83.1
	4	10.78	79	192	3.1	76.5
	8	6.10	133	367	5.4	67.6
	16	3.88	241	847	8.5	53.1
	32	3.32	456	2323	10.0	31.1
33/32/64	1	71.28	59	141	1	100
	2	41.88	84	176	1.7	85.1
	4	23.10	125	262	3.1	77.1
	8	12.30	208	474	5.8	72.4
	16	6.87	374	1031	10.4	64.9
	32	4.93	703	2665	14.4	45.2
33/64/64	1	169.25	108	238	1	100
	2	91.17	146	280	1.9	92.8
	4	48.45	215	397	3.5	87.3
	8	25.30	353	682	6.7	83.6
	16	13.47	631	1388	12.6	78.6
	32	8.03	1185	3330	21.1	65.8
65/64/64	1	380.95	256	570	1	100
	2	206.38	373	693	1.8	92.3
	4	104.05	601	1012	3.7	91.5
	8	57.35	1058	1717	6.6	83.0
	16	29.63	1972	3275	12.9	80.3
	32	15.85	3800	6940	24.0	75.1

Data for 1000 time steps.

larger meshes, the communication overhead is only a smaller fraction of the total CPU time.

5. Application of OSIMS algorithm to non-axisymmetric viscoelastic Taylor–Couette flow

In order to identify the parametric window for time-dependent viscoelastic simulations, a linear stability analysis is performed. From this point onwards, we consider only the inner cylinder rotating ($Re_1 \equiv Re$) while the outer cylinder is kept stationary ($Re_2 = 0$). We choose $\beta = 0.8$ and gap ratios 0.912 and 0.8 used in previous experiments [26,27,43,44]. The effect of elasticity ($E \equiv De/Re$) on stability threshold is presented for gap ratio of 0.912 in Fig. 11 through a linear stability analysis. As shown in Fig. 11(a), the axisymmetric and stationary mode ($\xi = 0$) is the most unstable one only for low values of

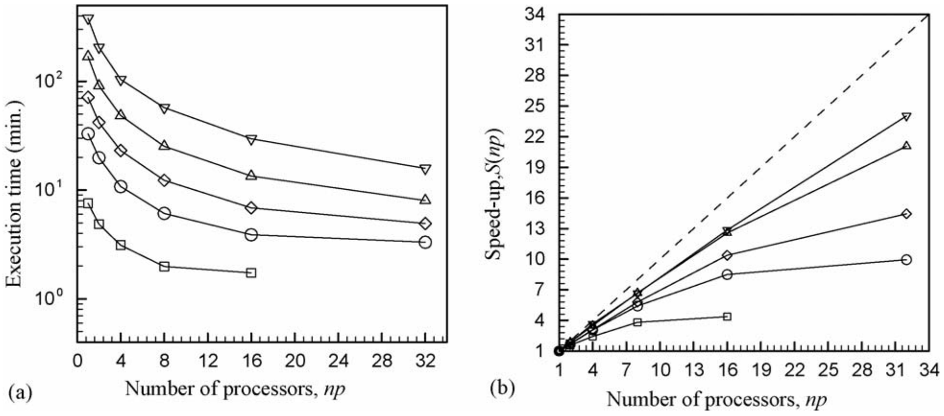

Fig. 10. Performance of parallel OSIMS program for 3D time-dependent viscoelastic flow simulation for 1000 time steps with mesh (r, z, θ) sizes: (□) 33 × 16 × 16, 33 × 32 × 32 (○), 33 × 32 × 64 (◇), 33 × 64 × 64 (△) and 65 × 64 × 64 (▽). (a) Semi-log plot of execution time (t(np) in min) vs. number of processors (np) and (b) speed-up (S(np)) vs. number of processors (np).

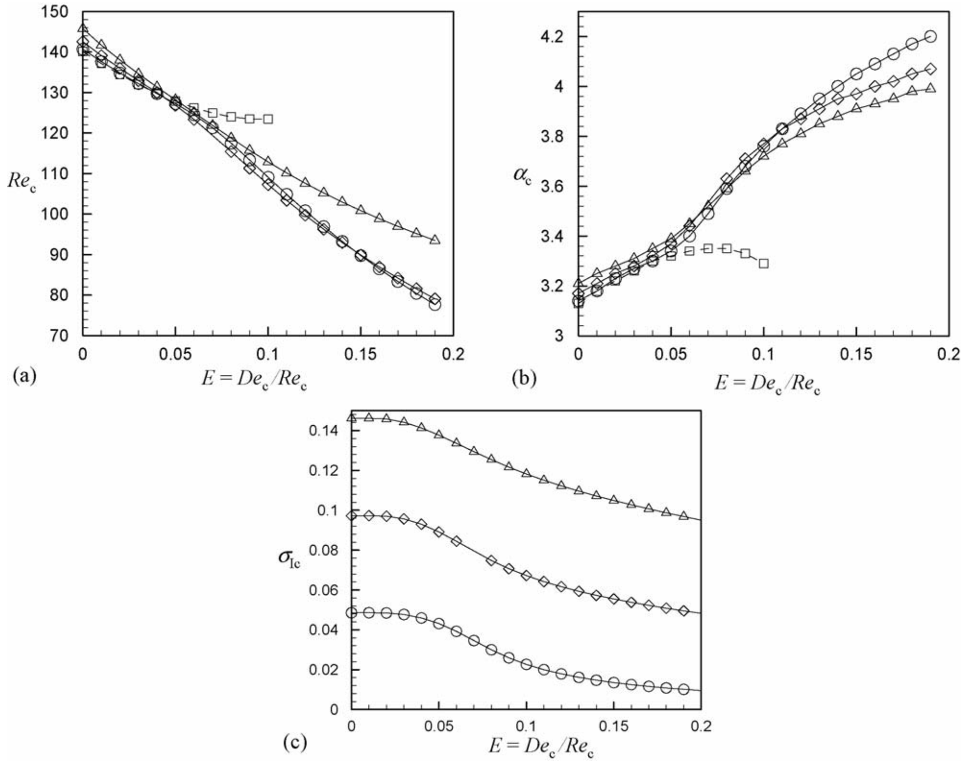

Fig. 11. Linear stability analysis of viscoelastic Taylor–Couette flow for $R_1/R_2 = 0.912$, $\beta = 0.8$, (□) $\xi = 0$, (◯) $\xi = 1$, (◇) $\xi = 2$, (△) $\xi = 3$. (a) Critical Reynolds number (Re_c) vs. elasticity number (E), (b) critical axial wave number (α_c) vs. elasticity number (E) and (c) critical angular frequency (σ_{Ic}) vs. elasticity number (E). Dashed and solid lines correspond to stationary and time-dependent modes, respectively.

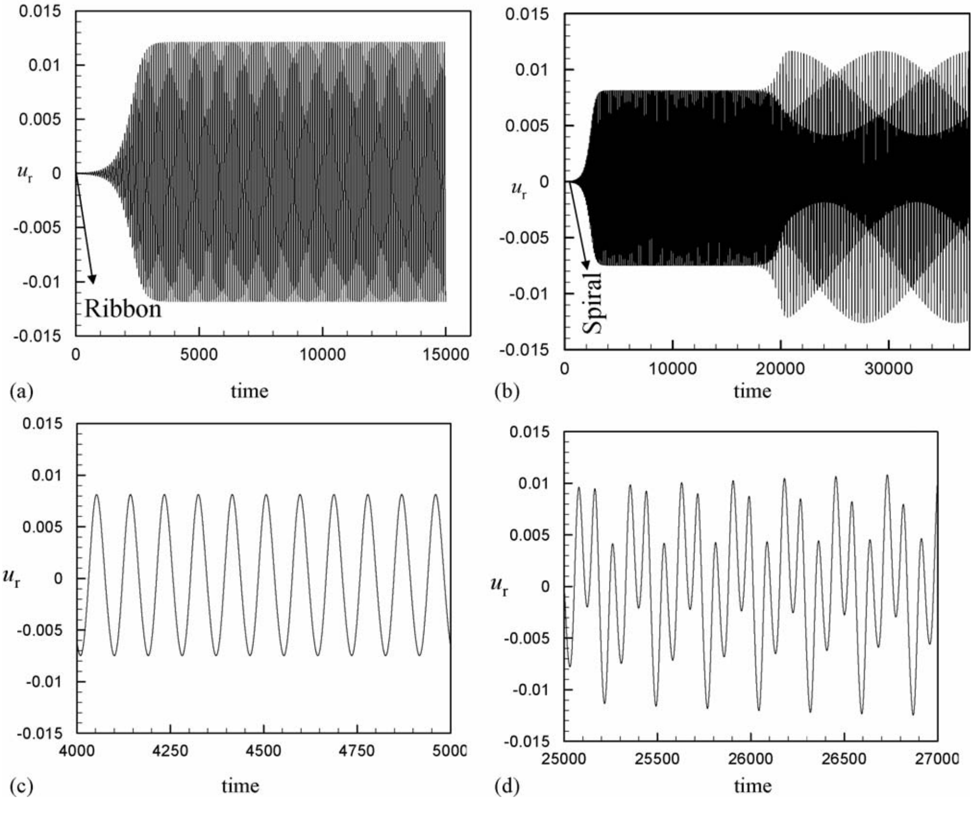

Fig. 12. Time evolution of radial velocity for viscoelastic Taylor–Couette flow at the center of the computational domain ($r = (r_1 + r_2)/2$, $\theta = \pi$, $z = \pi/\alpha$) for $R_1/R_2 = 0.912$, $\alpha = 3.7$, $Re = 114$, $De = 10$, $\xi = 2$. (a) Ribbon flow initial condition, (b) spiral flow initial condition, (c) velocity fluctuations of spirals of Fig. 12(b) and (d) velocity fluctuations of modulated spirals of Fig. 12(b). All initial conditions are superimposed over the steady state solution.

E while for $0.05 \leq E \leq 0.15$, the most unstable mode becomes non-axisymmetric and time-dependent with $\xi = 2$. For values of elasticity numbers greater than 0.15 the unstable mode corresponds to $\xi = 1$. The plot of the critical axial wavenumber α_c versus E in Fig. 11(b) shows that α_c varies within 3.15 and 4.2 in the range $0 \leq E \leq 0.2$. The temporal period, $2\pi/\sigma_{Ic}$, associated with the eigenfunctions of the time-dependent modes corresponding to the critical imaginary eigenvalue, σ_{Ic}, is of O(10) with respect to the time scale $d/R_1\Omega_1$ as shown in Fig. 11(c).

Time-dependent simulations are first performed using 33, 16 and 16 mesh points in r, z and θ directions respectively with $\Delta t = 0.05$ for $Re = 114$, $De = 10$, $\alpha = 3.7$ ($\xi = 2$). The initial solution corresponds to either of the two critical eigenfunctions: ribbon (Fig. 12(a)) or spiral (Fig. 12(b)). As shown in Fig. 12, the ribbon solution reaches a final time-periodic state while the spiral solution becomes unstable giving rise to a modulated spiral state with multiple frequencies. From the radial velocity contour plots of the final ribbon state of Fig. 12(a), it is evident that the ribbons are periodic with axial and azimuthal periods of $2\pi/\alpha_c$ and π, respectively (Fig. 13(a) and (b)), as predicted by LSA. Contour plots at time = 10,000 (spirals of Fig. 14(a) and (b)) and at time = 30,000 (modulated spirals of Fig. 14(d) and (e)) reveal the same spatial periodicity. The axial velocity (θ–z contour plot) in Fig. 13(c) indicates that the final state corresponds to ribbon pattern as compared to the spiral in Fig. 14(c) and modulated spiral in Fig. 14(g). From bifurcation analysis, it is seen that the bifurcations for both the ribbons and the spirals are supercritical with an amplitude proportional to the square-root of $Re - Re_c$ as shown in Fig. 15, and the time-dependent simulation reveals that the ribbon is the asymptotically stable pattern since the spiral becomes unstable for long times via an amplitude modulation.

In Fig. 16, we present LSA results for the viscoelastic TC flow of gap ratio $R_1/R_2 = 0.8$ for a range of elasticity numbers between 0 and 0.2. For low values of E, the axisymmetric modes ($\xi = 0$) are the most unstable ones while for $E > 0.03$, $\xi = 1$ (time-dependent) is the most unstable mode as plotted in Fig. 16(a). The axial wavenumber is also plotted against E in Fig. 16(b) and has a value that ranges between 3.1 and 4.2 for $0 \leq E \leq 0.2$. Note that the axisymmetric mode is stationary for $E \leq 0.1$ beyond which it is time-dependent with a time-period, $2\pi/\sigma_{Ic}$, of O(10) compared to the flow time scale, $d/R_1\Omega_1$ as shown in Fig. 16(c).

For the case $R_1/R_2 = 0.8$ and $\beta = 0.8$, time-dependent simulations are performed to investigate the limiting elasticity number below which the OSIMS algorithm can be employed without

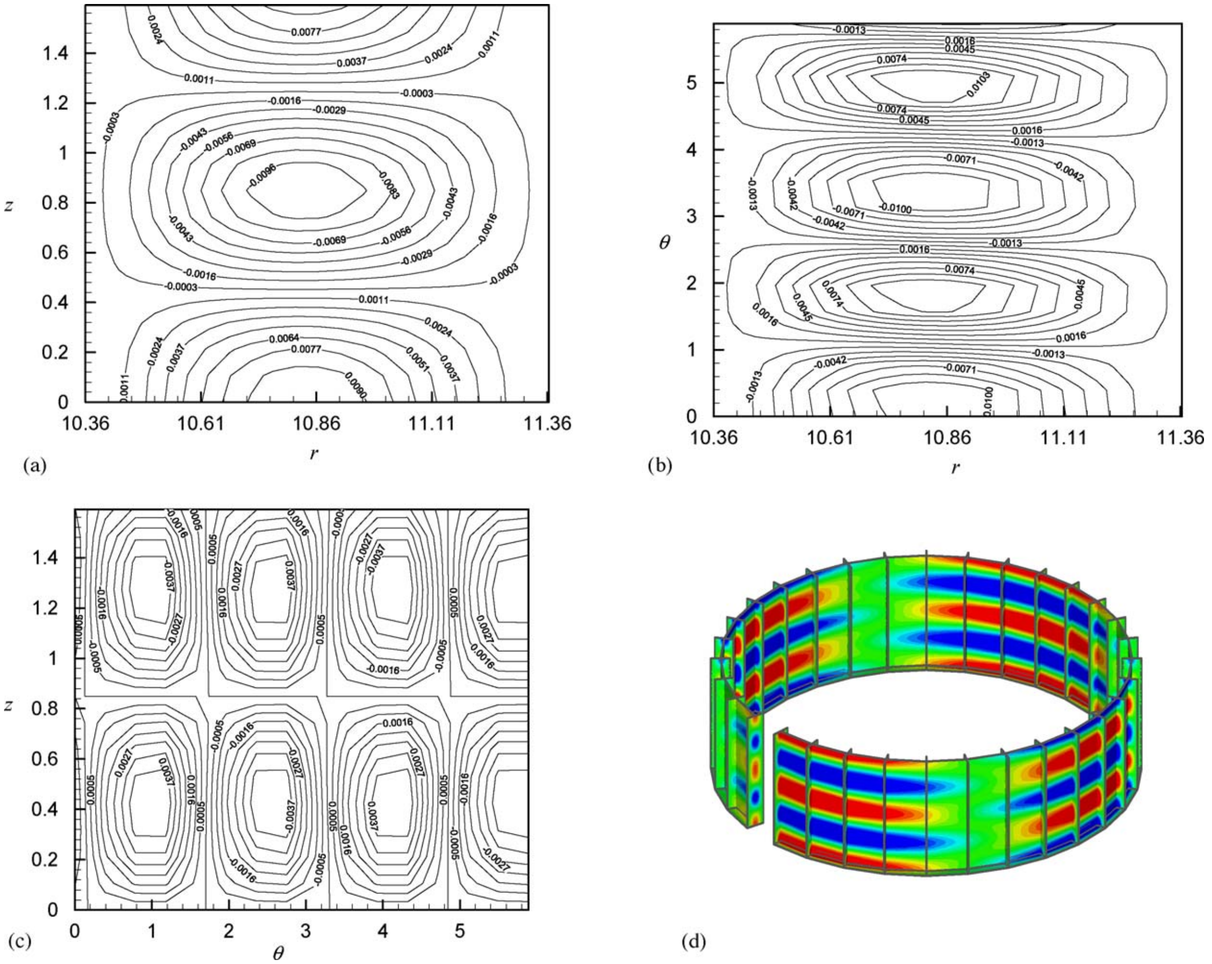

Fig. 13. Secondary flow contour plots of viscoelastic Taylor–Couette flow ($\xi = 2$) for $R_1/R_2 = 0.912$, $\alpha = 3.7$, $Re = 114$ and $De = 10$ corresponding to final ribbon pattern of Fig. 12(a). (a) Radial velocity (u_r) in r–z plane ($\theta = \pi$), (b) radial velocity (u_r) in r–θ plane ($z = \pi/\alpha$), (c) axial velocity (u_z) in θ–z plane ($r = (r_1 + r_2)/2$) and (d) 3D snapshot of u_r.

numerical instabilities that are expected to occur in semi-implicit schemes for viscoelastic flows [62]. The OSIMS algorithm successfully simulated flows for $E < 0.15$. Results are presented for values of $E = 0.03$, 0.05, 0.1, 0.125 and 0.15 slightly above the linear stability threshold, using 33, 16 and 16 mesh points in the radial, axial and azimuthal directions with a time step $\Delta t = 0.05$. Note that that all the results presented here for mesh size $33 \times 16 \times 16$ remain unchanged when the mesh was refined to $33 \times 32 \times 32$. For the case when $E = 0.03$ ($Re = 89.5$, $\alpha = 3.26$) as shown in Fig. 17, time-dependent simulations based on random initial conditions show that the secondary flow is axisymmetric and stationary, resembling TVF with an axial period $2\pi/\alpha_c$ as evident from the inset (r–z contour plots of the final radial and axial velocities at $\theta = \pi$). For $E = 0.05$ ($Re = 86.6$, $\alpha = 3.4$), the critical disturbance is non-axisymmetric ($\xi = 1$) and time-dependent (Fig. 16(a)). Hence two secondary flow patterns, namely ribbon or spiral can emerge at or above the stability threshold [36,38]. Time-dependent simulations were performed by using initial (Fig. 18) disturbances constructed from eigenfunctions of spiral and ribbon patterns. Irrespective of the initial condition, we observe that the final state corresponds to the ribbon pattern with $\xi = 1$. The r–z, r–θ and θ–z plane contour plots for radial and axial velocities corresponding to the final ribbon state of Fig. 18(a) are shown in Fig. 19. The spiral solution becomes unstable for long times and evolves into ribbon as shown in Fig. 18(b), and the θ–z contour plots of axial velocity represent spirals at time = 8000 and ribbons in the final state in Fig. 20(a) and (b), respectively. The bifurcation to the ribbon and spiral is supercritical as shown in Fig. 21, indicating that one of the two solutions is stable, which in this case happens to be the ribbon [12].

Time-dependent simulations for the ribbon state were also successfully performed for values of $E = 0.1$ ($Re = 72.0$, $\alpha = 3.85$) and 0.125 ($Re = 64.8$, $\alpha = 4.0$) as shown in Fig. 22(a) and (b), respectively. The final ribbon solution from simulations with $E = 0.05$ was used as initial solution for simulation with $E = 0.1$, and subsequently, the simulation for $E = 0.125$ was started using the final solution of $E = 0.1$. The bifurcation analyses show that the ribbons bifurcate subcritically for both $E = 0.1$ and 0.125 (see Fig. 23). Subcritical bifurcation to non-axisymmetric and

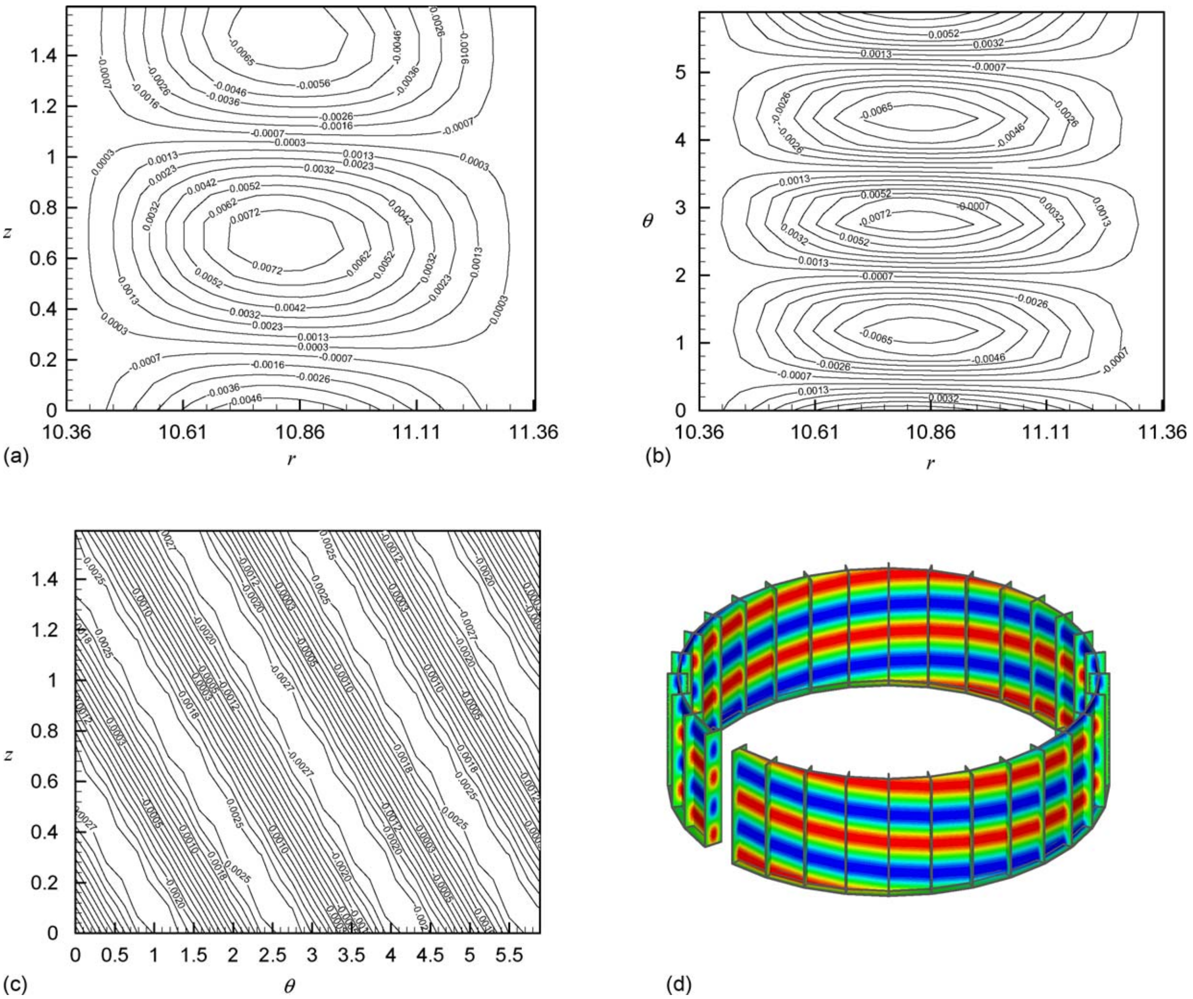

Fig. 14. Secondary flow contour plots of viscoelastic Taylor–Couette flow ($\xi = 2$) for $R_1/R_2 = 0.912$, $\alpha = 3.7$, $Re = 114$ and $De = 10$ with spiral initial condition of Fig. 12(b). (a) Radial velocity (u_r) in r–z plane ($\theta = \pi$) at time = 10,000, (b) radial velocity (u_r) in r–θ plane ($z = \pi/\alpha$) at time = 10,000, (c) axial velocity (u_z) in θ–z plane ($r = (r_1 + r_2)/2$) at time = 10,000, (d) 3D snapshot of u_r at time = 10,000 (e) radial velocity (u_r) in r–z plane ($\theta = \pi$) at time = 30,000, (f) radial velocity (u_r) in r–θ plane ($z = \pi/\alpha$) at time = 30,000, (g) axial velocity (u_z) in θ–z plane ($r = (r_1 + r_2)/2$) at time = 30,000 and (h) 3D snapshot of u_r at time = 30,000.

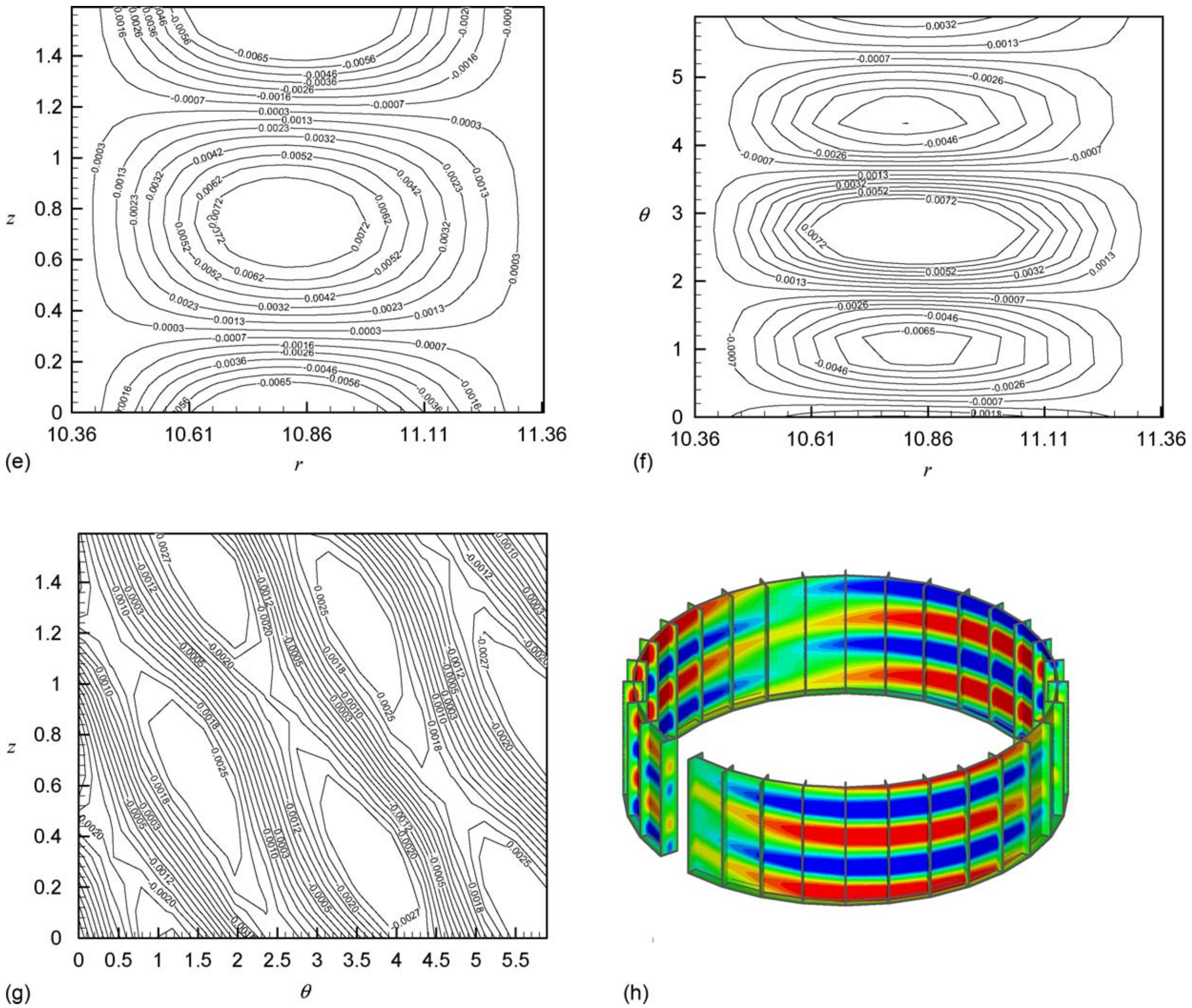

Fig. 14. (*Continued*).

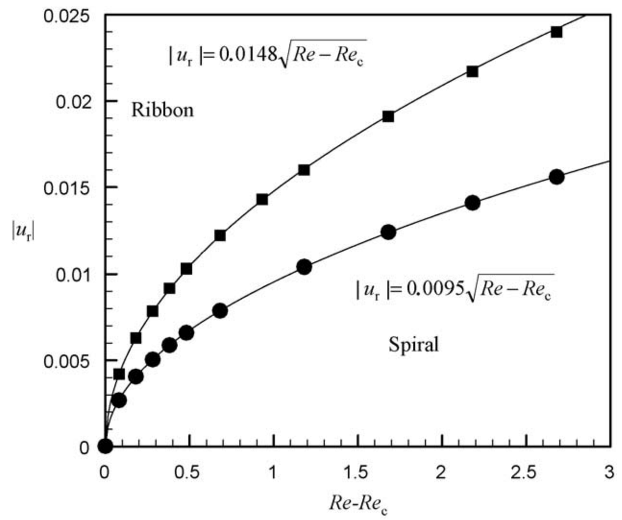

Fig. 15. Bifurcation diagram of final radial velocity (u_r) amplitude of viscoelastic Taylor–Couette flow ($\xi = 2$) corresponding to ribbons and spirals at the center of the computational domain ($r = (r_1 + r_2)/2$, $\theta = \pi$, $z = \pi/\alpha$) for $R_1/R_2 = 0.912$, $\alpha = 3.7$, $Re_c = 111.32$ and $De = 10$.

time-periodic states in viscoelastic flows has been predicted by local nonlinear analysis by Sureshkumar et al. [38] who enforced the spatio-temporal symmetries of the spiral and ribbon into a spectral numerical algorithm based on the Newton–Raphson technique. Bifurcation theory in presence of symmetries indicates that under such conditions neither of the two families is stable. However, we observe stable, ribbon-like patterns for sufficiently long times. It is plausible that this state is established through a limit point transition at high amplitudes, as conjectured by Sureshkumar et al. [38].

As shown in Fig. 24, for $E = 0.15$ ($Re = 59.333$, $\alpha = 4.05$), continuation from the final state at $E = 0.125$, failed after a few hundred time steps due to inception of numerical instabilities. The numerical instability did not disappear even after reducing the time step from 0.05 to 0.01 or refining the mesh size (r, z, θ) from $33 \times 16 \times 16$ to $33 \times 32 \times 32$. These numerical instabilities are commonly encountered in viscoelastic flow simulations [4,52,53,62] where the operator splitting errors lead to the loss of positive definiteness of the stress conformation tensor. In the following section, we investigate the use of an artificial stress diffusivity term introduced into the constitutive equation to overcome the numerical instability.

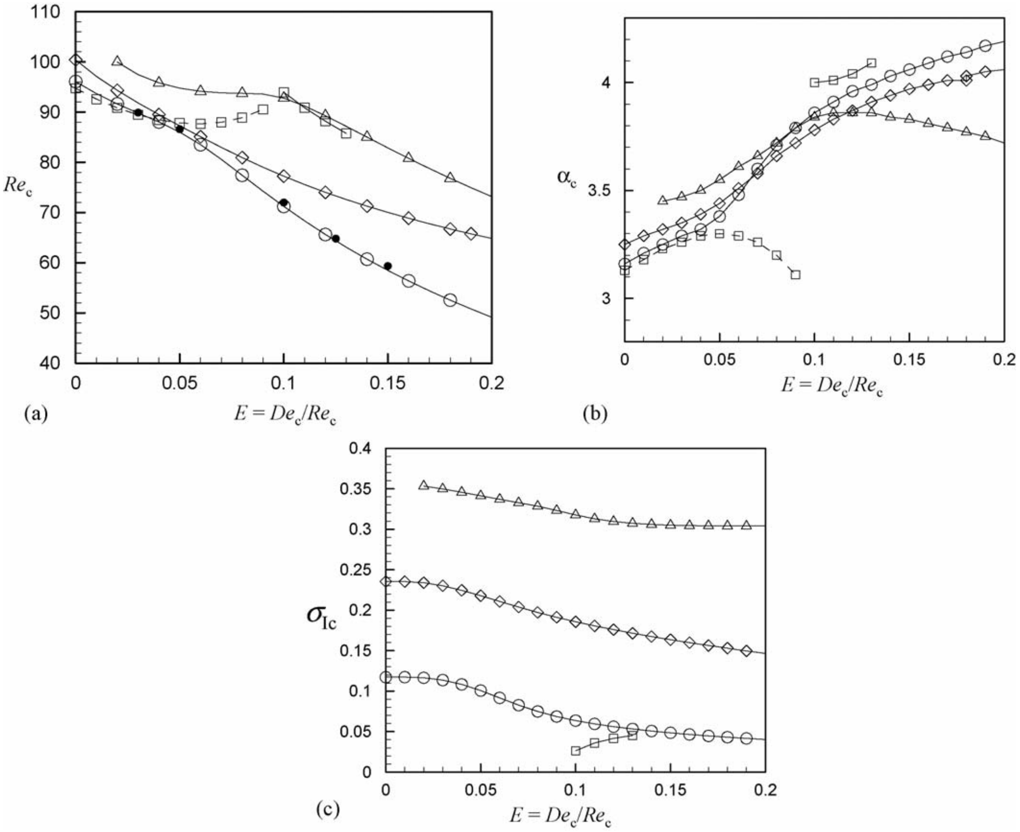

Fig. 16. Linear stability analysis of viscoelastic Taylor–Couette flow for $R_1/R_2=0.8$, $\beta=0.8$, (□) $\xi=0$, (◯) $\xi=1$, (◇) $\xi=2$, (△) $\xi=3$. (a) Critical Reynolds number (Re_c) vs. elasticity number (E), (b) critical axial wave number (α_c) vs. elasticity number (E) and (c) critical angular frequency (σ_{Ic}) vs. elasticity number (E). Dashed and solid lines correspond to stationary and time-dependent modes, respectively. Filled dots correspond to points chosen for time-dependent simulations.

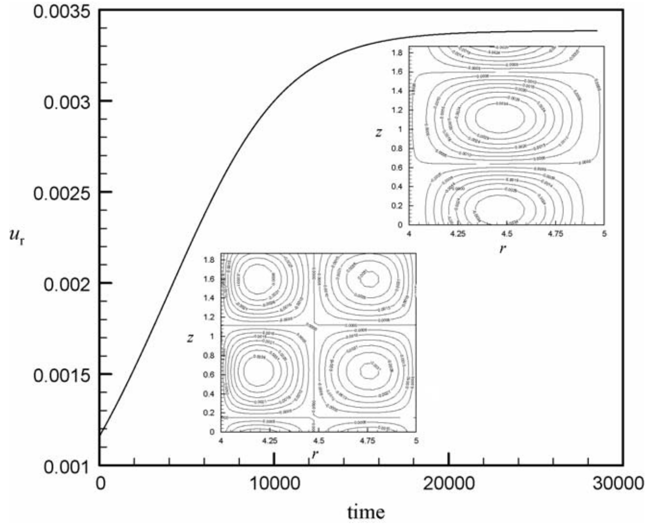

Fig. 17. Time evolution of radial velocity for axisymmetric ($\xi=0$) viscoelastic Taylor–Couette flow at the center of the computational domain ($r=(r_1+r_2)/2$, $\theta=\pi$, $z=\pi/\alpha$) for $R_1/R_2=0.8$, $\beta=0.8$, $\alpha=3.26$, $Re=89.5$, $E=De/Re=0.03$. Inset figures correspond to r–z plane contours ($\theta=\pi$) of axial velocity, u_z (bottom) and radial velocity, u_r (top) at the final stationary state.

6. Effect of artificial stress diffusivity

Introducing small amounts of artificial stress diffusion into the hyperbolic stress constitutive equation has been proved to be successful in earlier studies [4,53,62] which used operator splitting algorithms in viscoelastic turbulent channel flow simulations. Specifically, the presence of small amounts of artificial stress diffusion made it possible for time integrating the mixed elliptic–hyperbolic set of equations over longer periods of time, which would otherwise be affected by numerical instabilities. Note that such an artificial diffusive scheme has not been implemented for curvilinear viscoelastic flows such as the Taylor–Couette flow. The scheme is implemented by adding a stress diffusion term, involving a constant scalar diffusivity κ (dimensionless w.r.t. $R_1\Omega_1 d$), into the Oldroyd-B Eq. (3) as given by

$$\boldsymbol{\tau}_{(1)} = -\frac{1}{De}[\boldsymbol{\tau} - (\nabla \mathbf{u} + (\nabla \mathbf{u})^t)] + \kappa \nabla^2 \boldsymbol{\tau}. \tag{18}$$

The scalar diffusion coefficient κ should be selected such that stable time-integration is achieved without qualitatively influencing the flow dynamics. In the simulations, we follow a general criteria for choosing the magnitude of stress diffusivity (κ) based upon the fact that $\kappa(R_1\Omega_1 d)/\nu \ll 1$ and $\kappa(R_1\Omega_1 d)/(d^2/\lambda) \ll 1$, where ν is the total kinematic viscosity (η_T/ρ). In other words,

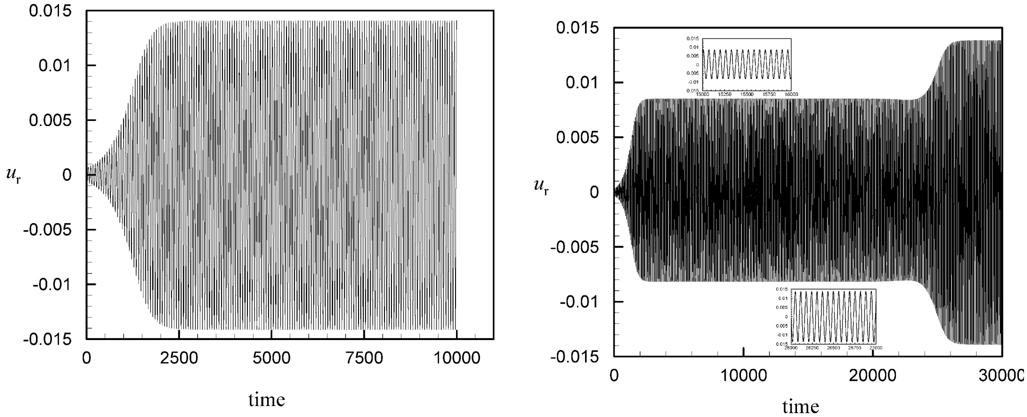

(a) (b)

Fig. 18. Time evolution of radial velocity for non-axisymmetric ($\xi = 1$) viscoelastic Taylor–Couette flow at the center of the computational domain ($r = (r_1 + r_2)/2$, $\theta = \pi$, $z = \pi/\alpha$) for $R_1/R_2 = 0.8$, $\beta = 0.8$, $\alpha = 3.4$, $Re = 86.6$, $E = De/Re = 0.05$. (a) Ribbon flow initial condition and (b) spiral flow initial condition. All initial conditions are superimposed over the steady state solution. Final pattern corresponds to ribbon in both cases.

the value of κ is to be selected such that $\kappa Re \ll 1$ and $\kappa De \ll 1$. The former may be thought of as inverse of a Schmidt number Sc_κ defined as the ratio of the kinematic viscosity to (dimensional) stress diffusivity. In DNS of channel flow, typical values of $Sc_\kappa \cong 0.3$. The values of Sc_κ used here range between 8.33 and 16.67.

The evolution equation of the modified Oldroyd-B (Eq. (18)) is time-integrated first based on the Adams–Bashforth second order explicit scheme in the absence of artificial diffusion, given as

$$\frac{\boldsymbol{\tau}^{n+1/2} - \boldsymbol{\tau}^{n}}{\Delta t} = \frac{3}{2} f(\boldsymbol{\tau}^{n}, \boldsymbol{u}^{n}) - \frac{1}{2} f(\boldsymbol{\tau}^{n-1}, \mathbf{u}^{n-1}), \tag{19}$$

where f is given by Eq. (14).

This is followed by solving implicitly for the polymeric stress ($\boldsymbol{\tau}^{n+1}$) at the ($n+1$)th time step, with inclusion of the stress diffusion term, given as

$$(\nabla^2 \boldsymbol{\tau})^{n+1} - \frac{2}{\kappa \Delta t} \boldsymbol{\tau}^{n+1} = -(\nabla^2 \boldsymbol{\tau})^{n} - \frac{2}{\kappa \Delta t} \boldsymbol{\tau}^{n+1/2}. \tag{20}$$

Eq. (20) is supplemented with wall boundary conditions $\boldsymbol{\tau}^{n+1} = \boldsymbol{\tau}^{n+1/2}$ at $r = r_1$ and $r = r_2$.

Using the diffusive OSIMS algorithm, we first examine the linear stability problem to examine the influence of stress diffusivity on the leading mesh-converged eigenvalues. It is also important to examine the effect of diffusivity on the two continuous sets of eigenvalues of the Oldroyd-B model, whose real parts are equal to $-1/De$ and $-1/(\beta De)$. The eigenfunctions corresponding to these eigenvalues exhibit highly singular behavior and are difficult to be resolved numerically [63]. Finally, it is essential to verify that the introduction of finite κ does not result in "spurious" eigenvalues on the positive half plane. Two test cases in the Re versus E diagram (see Fig. 16(a)) are chosen for the present study—one close to the stability boundary ($E = 0.15$, $Re = 59.333$, $\alpha = 4.05$) at which numerical break-down occurred in the absence of diffusivity as shown in Fig. 24, and the other well beyond the stability threshold ($E = 0.033$, $Re = 120$, $\alpha = 4.0$). In Fig. 25(a), we compare the eigenspectrum for $E = 0.15$ ($Re = 59.333$, $\alpha = 4.05$, $\xi = 1$) both in the absence and presence of stress diffusivity ($\kappa = 10^{-4}$, 10^{-3}). As seen from there, the presence of artificial diffusivity destroys the continuous spectra and causes the real part of the eigenvalues contained in them to become more negative. This is consistent with the observations made by Sureshkumar and Beris for plane Poiseuille flow [53]. Moreover, the leading eigenvalue remains practically unaffected when $\kappa = 10^{-4}$ although a (95%) shift towards the stable region is observed, when κ is raised to 10^{-3}. Thus, stress diffusivity has a stabilizing effect on the linearly perturbed flow. We also see that the artificial stress diffusivity does not give rise to any spurious eigenvalues in the unstable region, which is an encouraging result from the view point of finite-amplitude simulations. Similar observations were also made for $E = 0.033$ (Fig. 25(b)).

We now present results for the nonlinear dynamics predicted by the diffusive OSIMS algorithm. A value of $\kappa = 10^{-4}$ was sufficient to overcome the numerical instability as clearly shown in the time-dependent simulation result plotted in Fig. 26(a). The final state corresponds to the ribbon pattern as evident from the θ–z contour plot of u_z in Fig. 26(b). In order to ascertain the effect of κ on the temporal evolution of the disturbances and pattern selection, we compared the dynamics predicted by the diffusive and non-diffusive OSIMS algorithm. We chose to perform simulations at $E = 0.033$ ($Re = 120$, $De = 4$, $\alpha = 4.0$, $\xi = 1$) at which the latter algorithm was numerically stable, by using as initial condition the stable ribbon state obtained for $E = 0.125$ ($Re = 64.8$, $De = 8.1$, $\alpha = 4.0$, $\xi = 1$), reported in Fig. 22(b). The temporal evolution predicted by the two algorithms is shown in Fig. 27(a) and (b) while θ–z contour plots of the asymptotic stable states are compared in Fig. 28(a) and (b). As evident from Figs. 27 and 28, the final stable states are axially traveling spirals in the diffusive and non-diffusive simulations. Thus, the diffusive algorithm is able to capture the final stable spiral pattern of the non-diffusive simulation, although the ribbon ($E = 0.125$) to spiral transition time occurs earlier in the presence of stress diffusion as seen in Fig. 27(a) and (b). The advancement in the transition time from ribbon to spiral can be understood as fol-

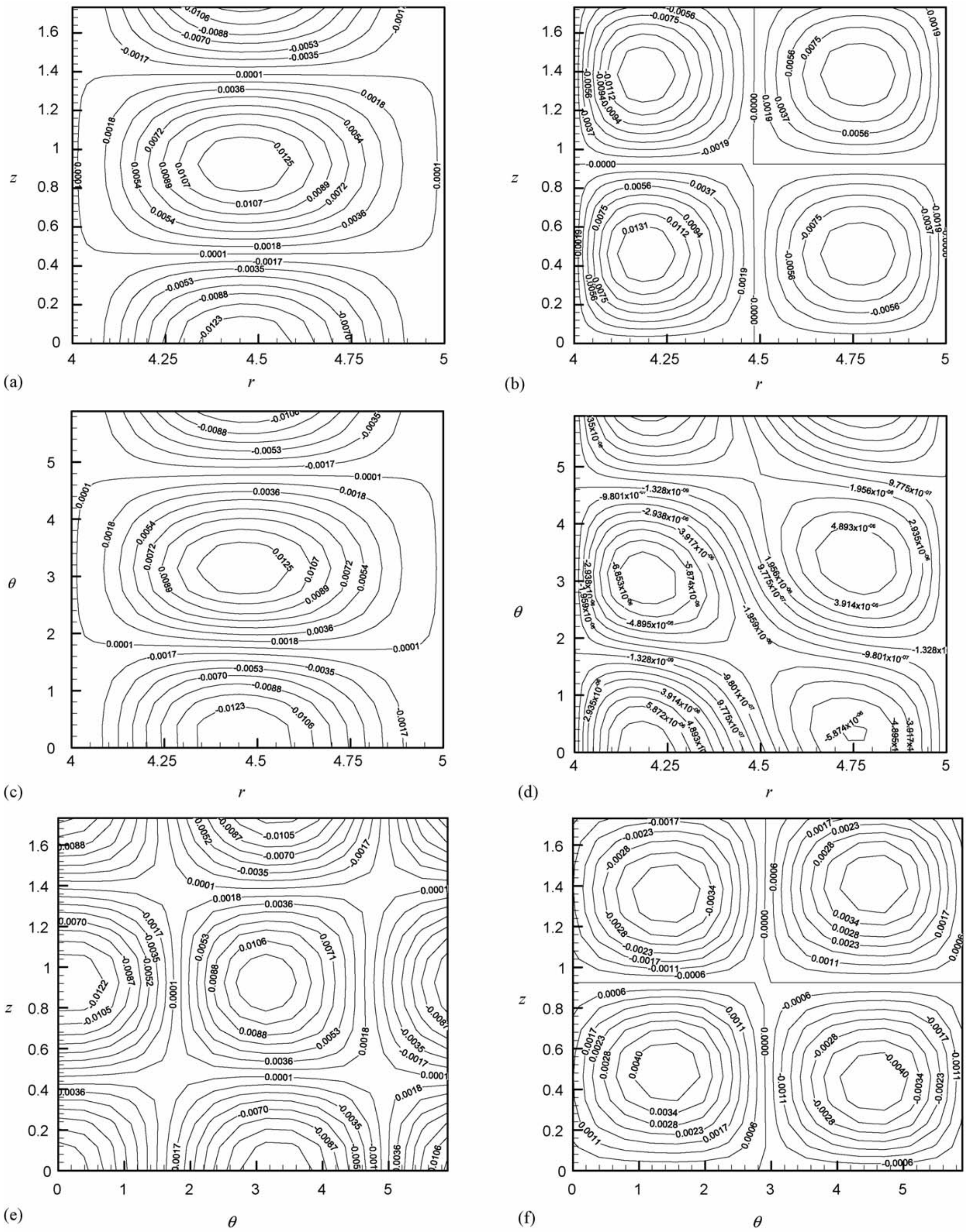

Fig. 19. Secondary flow contour plots of viscoelastic Taylor–Couette flow ($\xi = 1$) for $R_1/R_2 = 0.8$, $\beta = 0.8$, $\alpha = 3.4$, $Re = 86.6$ and $E = De/Re = 0.05$ corresponding to final ribbon pattern of Fig. 18(a). (a) Radial velocity (u_r) in r–z plane ($\theta = \pi$), (b) axial velocity (u_z) in r–z plane ($\theta = \pi$), (c) radial velocity (u_r) in r–θ plane ($z = \pi/\alpha$), (d) axial velocity (u_z) in r–θ plane ($z = \pi/\alpha$), (e) radial velocity (u_r) in θ–z plane ($r = (r_1 + r_2)/2$) and (f) axial velocity (u_z) in θ–z plane ($r = (r_1 + r_2)/2$).

lows. It is expected that the magnitudes of the velocities and stresses should change due to decrease in the elasticity from 0.125 to 0.033. The elastic forces are therefore reduced, and the flow adjusts itself to the stable spiral pattern which is a modification of the Newtonian flow. The presence of small amounts of diffusion will have a dampening effect on the magnitude of the stresses which through the elasticity term in the momentum equation (Eq. (1)) can cause the velocity flow field to adjust itself

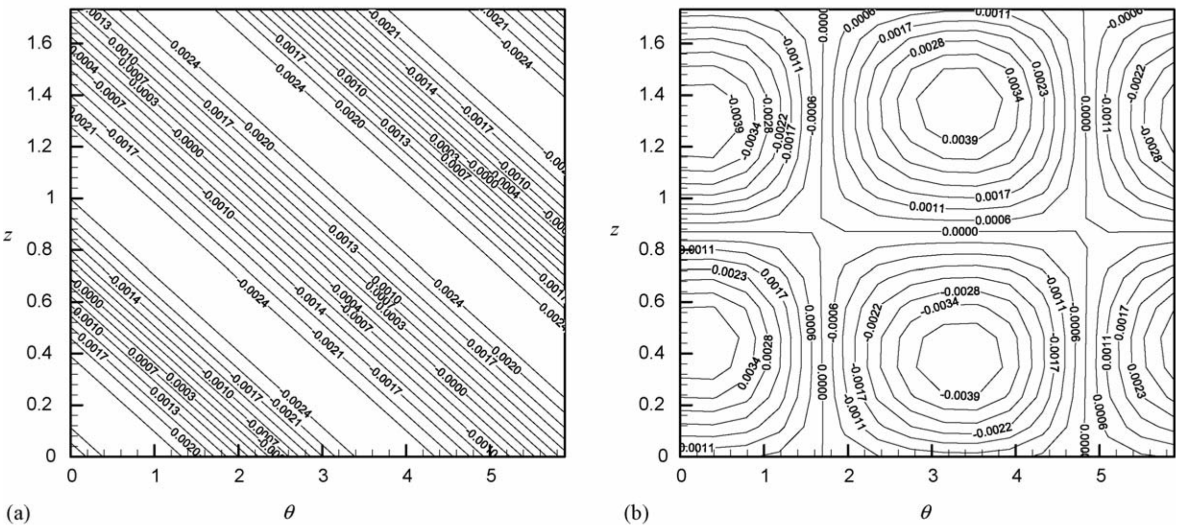

Fig. 20. Secondary flow contour plots of viscoelastic Taylor–Couette flow ($\xi = 1$) for $R_1/R_2 = 0.8$, $\beta = 0.8$, $\alpha = 3.4$, $Re = 86.6$ and $E = De/Re = 0.05$ with spiral initial condition of Fig. 18(b). (a) Axial velocity (u_z) in θ–z plane ($r = (r_1 + r_2)/2$) corresponding to spiral state about time = 8000 and (b) axial velocity (u_z) in θ–z plane ($r = (r_1 + r_2)/2$) corresponding to final ribbon pattern.

faster (in this case) or slower to reach the stable state depending upon the growth/dissipation of mean flow energy necessary to sustain the new flow state. It is also to be noted that no information about the actual flow dynamics is lost in presence of small amounts of stress diffusion, except on the onset time of flow state transition. Generally, depending on the nonlinear interplay between inertial, viscous and elastic forces in the flow and also on the pattern (spatio-temporal)/strength (mean flow energy) of the initial flow state, the flow can either transition to a different pattern or remain the same with modification in the stress, velocity or energy amplitudes. The sequence of transitions to the final stable pattern and the time for these transitions depend on the initial solution used and the energy contained in the mean flow. For example, the base Couette flow cannot change to TVF by increasing the flow parameters beyond the critical values without adding sufficient amount of finite-amplitude disturbances (energy) to the base flow to start with. Hence, introduction of stress diffusivity allows us to circumvent the numerical instabilities for simulation of flows with high elasticity without affecting the flow dynamics appreciably.

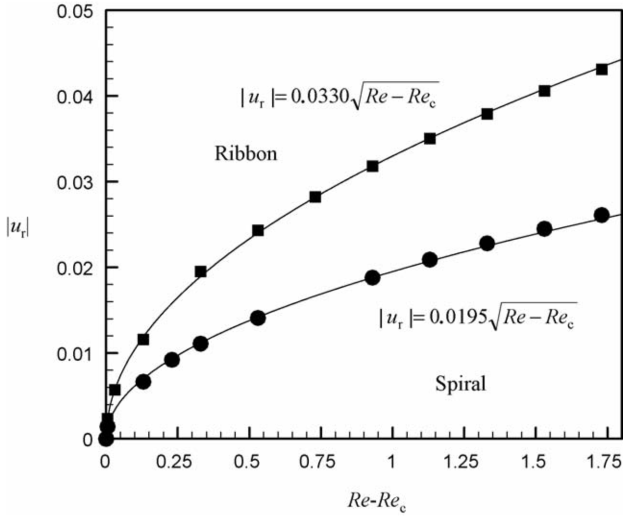

Fig. 21. Bifurcation diagram of final radial velocity (u_r) amplitude of viscoelastic Taylor–Couette flow ($\xi = 1$) corresponding to ribbons and spirals at the center of the computational domain ($r = (r_1 + r_2)/2$, $\theta = \pi$, $z = \pi/\alpha$) for $R_1/R_2 = 0.8$, $\beta = 0.8$, $\alpha = 3.4$, $Re_c = 85.87$ and $De = 4.33$.

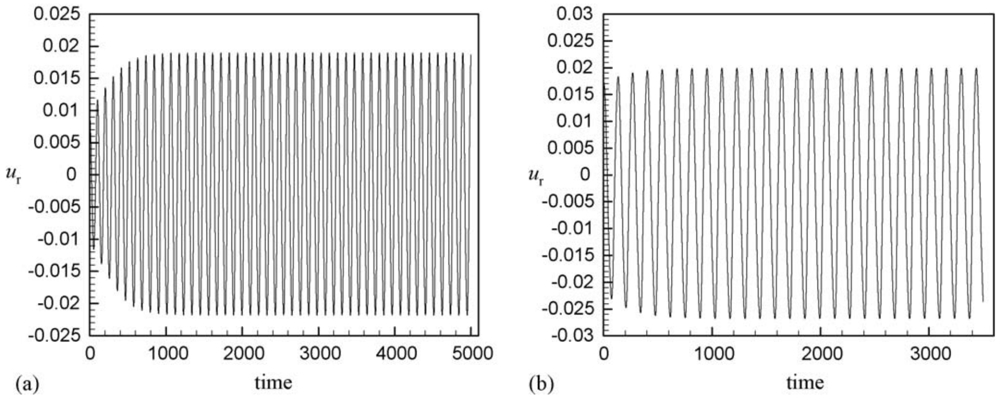

Fig. 22. Time evolution of radial velocity for viscoelastic Taylor–Couette flow ($\xi = 1$) at the center of the computational domain ($r = (r_1 + r_2)/2$, $\theta = \pi$, $z = \pi/\alpha$) for $R_1/R_2 = 0.8$, $\beta = 0.8$. (a) $\alpha = 3.85$, $Re = 72.0$, $E = De/Re = 0.1$ (continued from ribbon state at $E = 0.05$) and (b) $\alpha = 4.0$, $Re = 64.8$, $E = De/Re = 0.125$ (continued from ribbon state at $E = 0.1$).

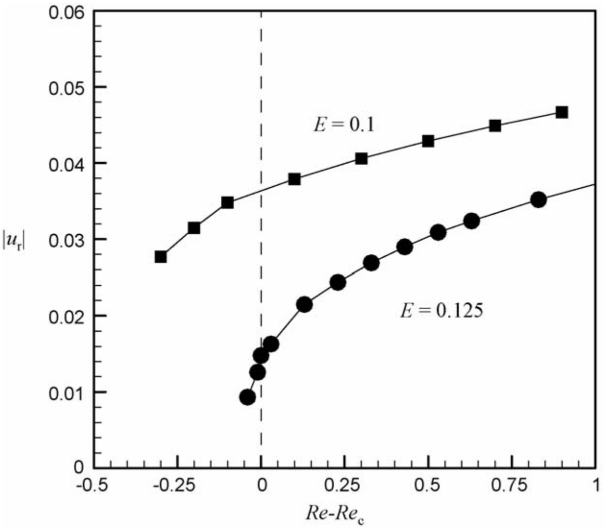

Fig. 23. Bifurcation diagram of final radial velocity (u_r) amplitude of viscoelastic Taylor–Couette flow ($\xi = 1$) corresponding to ribbons at the center of the computational domain ($r = (r_1 + r_2)/2$, $\theta = \pi$, $z = \pi/\alpha$) for $R_1/R_2 = 0.8$, $\beta = 0.8$. (a) $\alpha = 3.85$, $Re_c = 70.67$, $De = 7.2$ and (b) $\alpha = 4.0$, $Re_c = 63.9$ and $De = 8.1$.

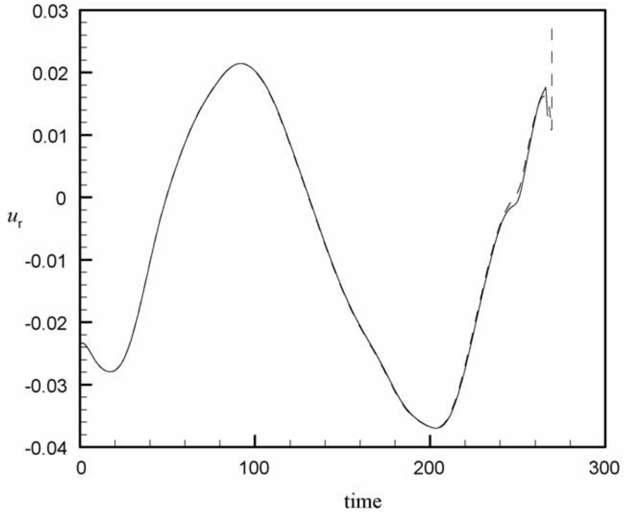

Fig. 24. Time evolution of radial velocity for viscoelastic Taylor–Couette flow ($\xi = 1$) at the center of the computational domain ($r = (r_1 + r_2)/2$, $\theta = \pi$, $z = \pi/\alpha$) for $R_1/R_2 = 0.8$, $\beta = 0.8$, $\alpha = 4.05$, $Re = 59.333$, $E = De/Re = 0.15$ (continued from ribbon state at $E = 0.125$, $\Delta t = 0.01$ (dashed line), 0.05 (solid line)).

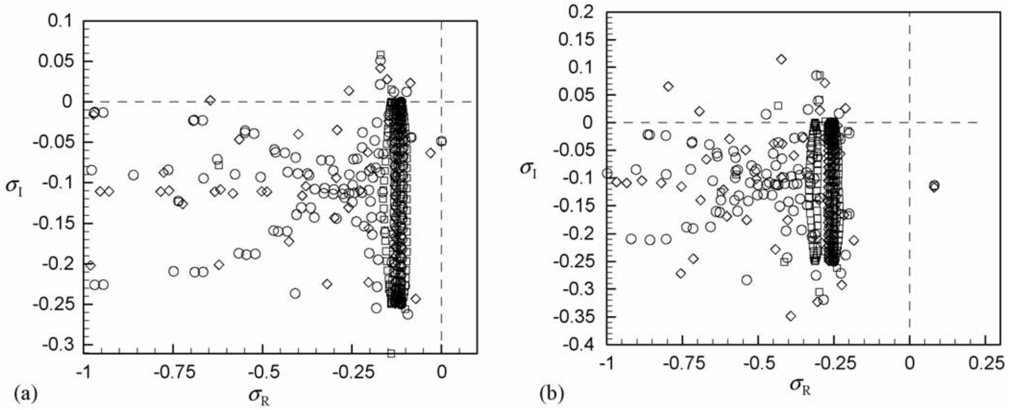

Fig. 25. Effect of artificial stress diffusivity on eigenspectrum ($R_1/R_2 = 0.8$). (a) $E = 0.15$, $Re = 59.333$, $\alpha = 4.05$ at (□) $\kappa = 0$, (◯) $\kappa = 10^{-4}$, (◇) $\kappa = 10^{-3}$ and (b) $Re = 120$, $De = 4$, $\alpha = 4.0$ at (□) $\kappa = 0$, (◯) $\kappa = 10^{-4}$, (◇) $\kappa = 10^{-3}$.

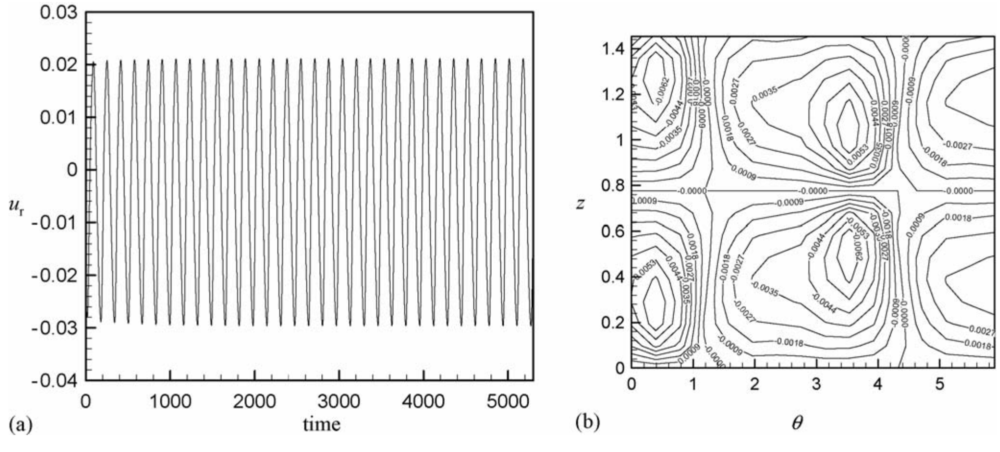

Fig. 26. Effect of artificial stress diffusivity for $E = 0.15$, $Re = 59.333$, $\alpha = 4.05$ with $\kappa = 10^{-4}$ ($R_1/R_2 = 0.8$, $\xi = 1$). (a) Time-dependent simulation with $\Delta t = 0.05$, $33 \times 16 \times 16$ mesh points in r, z, θ directions respectively and (b) contour plot of axial velocity (u_z) in θ–z plane ($r = (r_1 + r_2)/2$) corresponding to final ribbon pattern.

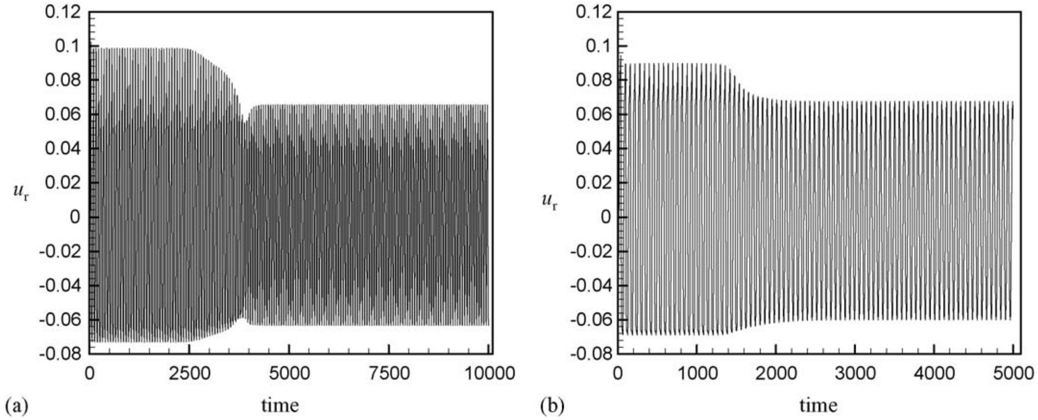

Fig. 27. Effect of artificial diffusivity for $Re = 120$, $De = 4$, $\alpha = 4.0$ ($R_1/R_2 = 0.8$, $\xi = 1$). (a) Time-dependent simulation with $\kappa = 0$ and (b) time-dependent simulation with $\kappa = 10^{-3}$. All initial conditions are from the final solution of $E = 0.125$ of Fig. 22(b). $\Delta t = 0.05$, $33 \times 16 \times 16$ mesh points in r, z and θ directions, respectively.

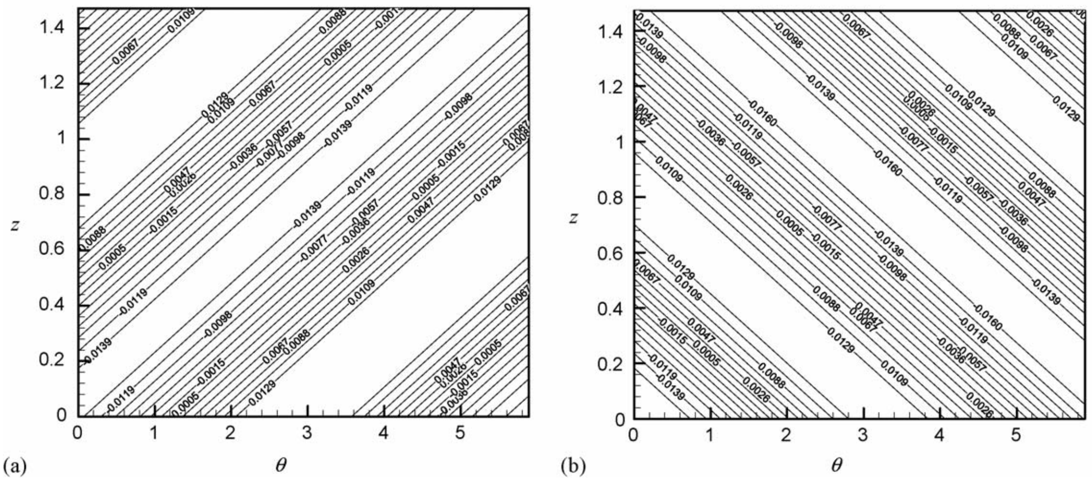

Fig. 28. Contour plot of axial velocity (u_z) in θ–z plane ($r = (r_1 + r_2)/2$) corresponding to final spiral pattern for $Re = 120$, $De = 4$, $\alpha = 4.0$ ($R_1/R_2 = 0.8$, $\xi = 1$). (a) $\kappa = 0$ and (b) $\kappa = 10^{-3}$.

7. Conclusions

We have implemented an operator-splitting influence matrix spectral (OSIMS) algorithm to simulate for the first time non-axisymmetric and time-dependent flow states in the viscoelastic Taylor–Couette flow of an Oldroyd-B liquid. The OSIMS algorithm is validated based on its predictions for the torque and finite amplitude states in axisymmetric Newtonian flows, which are in excellent agreement with previous experimental [61] and theoretical studies [13,17]. Moreover, the predictions of the dynamics near the bistability point (0, 1) for counter-rotating cylinders are also consistent with the findings of a bifurcation analysis in presence of symmetries [13] and the experimental observations of Andereck et al. [7].

The OSIMS algorithm is shown to be very memory and CPU efficient as both requirements scale linearly with L^2JK where L, J and K represents the number of mesh points used in the radial (Chebyshev), axial (Fourier) and azimuthal (Fourier) directions, respectively. Faster simulations were made possible by parallel implementation of the algorithm on a super-computing platform. For large degrees of freedom, $N_p > 2$ million, the parallel program performs very well with efficiency and speed-up increasing with increasing N_p. Specifically, for $N_p \approx 2.7$ million ($=10 \times 65 \times 64 \times 64$), the program runs at 75% efficiency with 32 processors. For $E \equiv De/Re \geq 0.15$, the OSIMS algorithm is prone to numerical instabilities. Hence, a diffusive version of OSIMS was developed by introducing an artificial stress diffusion, κ, into the Oldroyd-B constitutive equation. It was shown that small amount of stress diffusion (κRe or $\kappa De \ll 1$) allows for stable time-integration for larger E values. Moreover, for E values smaller than 0.15 for which the non-diffusive algorithm is numerical stable, its predictions are shown to be consistent with those obtained with artificial stress diffusion. In the scope of the present work, the largest elasticity value investigated using artificial stress diffusion is 0.15, but values of E as high as 0.3 can also be simulated based on our experience.

The pattern selection is shown to be dependent on E and the gap width. For a gap ratio (R_1/R_2) of 0.8, simulations show that the ribbon pattern is asymptotically stable as compared to the spiral for $E < 0.15$. However, for $R_1/R_2 = 0.912$, a modulated spiral flow with multiple frequencies is also observed. For $R_1/R_2 = 0.8$ and $E = 0.1$ and 0.125, the bifurcation to ribbons occurs through a subcritical transition while the transition is supercritical for smaller *E* values. It is plausible that higher-order transitions from the ribbon or spiral states could occur at larger *E* values leading to chaotic or disordered states seen experimentally [1,45,47,48].

Acknowledgements

We gratefully acknowledge the financial support for this research work from the NSF through grants CTS-9874813 and CTS-0335348.

References

[1] A. Groisman, V. Steinberg, Elastic turbulence in a polymer solution flow, Nature 405 (2000) 53.
[2] T. Vaithianathan, L.R. Collins, Numerical approach to simulating turbulent flow of a viscoelastic polymer solution, J. Comp. Phys. 187 (2003) 1.
[3] K.D. Housiadas, A.N. Beris, An efficient fully implicit spectral scheme for DNS of turbulent viscoelastic channel flow, J. Non-Newtonian Fluid Mech. 122 (2004) 243.
[4] R. Sureshkumar, A.N. Beris, R.A. Handler, Direct numerical simulation of the turbulent channel flow of a polymer solution, Phys. Fluids 9 (3) (1997) 743.
[5] P.G. Drazin, W.H. Reid, Hydrodynamic Stability, Cambridge University Press, 1981.
[6] G.I. Taylor, Stability of a viscous liquid contained between rotating cylinders, Phils. Trans. R. Soc. Lond. A 223 (1923) 289.
[7] C.D. Andereck, S.S. Liu, H.L. Swinney, Flow regimes in a circular Couette system with independently rotating cylinders, J. Fluid Mech. 164 (1986) 155.
[8] Y. Demay, G. Iooss, Calcul des solutions bifurquees pour la probleme de Couette-Taylor avec les deux cylinders en rotation, J. Mec. Theor. Appl. (1984) 193 (Special Issue).
[9] Y. Demay, G. Iooss, P. Laure, Wave patterns in the small gap Couette–Taylor problem, Eur. J. Mech. B 11 (1992) 621.
[10] H. Fasel, O. Booz, Numerical investigation of supercritical Taylor-vortex flow for a wide gap, J. Fluid Mech. 138 (1984) 21.
[11] P.R. Fenstermacher, H.L. Swinney, J.P. Gollub, Dynamic instabilities and the transition to chaotic Taylor vortex flow, J. Fluid Mech. 94 (1979) 103.
[12] M. Golubitsky, I.N. Stewart, Symmetry and stability in Taylor–Couette flow, SIAM J. Math. Anal. 17 (1986) 249.
[13] M. Golubitsky, W.F. Langford, Pattern formation and bistability in flow between counterrotating cylinders, Physica D 32 (1988) 362.
[14] C.B. Liao, S.J. Jane, D.L. Young, Numerical simulations of three dimensional Couette–Taylor flows, Int. J. Numer. Methods Fluids 29 (1999) 827.
[15] P.S. Marcus, Simulation of Taylor–Couette flow. Part 1. Numerical methods and comparison with experiment, J. Fluid Mech. 146 (1984) 45.
[16] P.S. Marcus, Simulation of Taylor–Couette flow. Part 2. Numerical results for wavy-vortex flow with one traveling wave, J. Fluid Mech. 146 (1984) 65.
[17] R.D. Moser, P. Moin, A. Leonard, A spectral numerical method for the Navier–Stokes equation with applications to Taylor–Couette flow, J. Comp. Phys. 52 (1983) 524.
[18] R.B. Bird, C.F. Curtiss, R.C. Armstrong, O. Hassager, Dynamics of Polymeric Liquids, vols. 1 and 2, 2nd ed., Wiley, New York, 1987.
[19] R.G. Larson, Instabilities in viscoelastic flows, Rheol. Acta 31 (1992) 213.
[20] R.G. Larson, E.S.G. Shaqfeh, S.J. Muller, A purely elastic instability in Taylor–Couette flow, J. Fluid Mech. 218 (1990) 573.
[21] S.J. Muller, E.S.G. Shaqfeh, R.G. Larson, Experimental studies of the onset of instability in viscoelastic Taylor–Couette flow, J. Non-Newtonian Fluid Mech. 46 (1993) 315.
[22] S.J. Muller, R.G. Larson, E.S.G. Shaqfeh, A purely elastic transition in Taylor–Couette flow, Rheol. Acta 28 (1989) 499.
[23] E.S.G. Shaqfeh, Purely elastic instabilities in viscometric flows, Annu. Rev. Fluid Mech. 28 (1996) 129.
[24] E.S.G. Shaqfeh, S.J. Muller, R.G. Larson, The effects of gap width and dilute solution properties on the viscoelastic Taylor–Couette instability, J. Fluid Mech. 235 (1992) 285.
[25] G.H. McKinley, P. Pakdel, A. Oeztekin, Rheological and geometric scaling of purely elastic flow instabilities, J. Non-Newtonian Fluid Mech. 467 (1996) 19.
[26] B.M. Baumert, S.J. Muller, Flow visualization of the elastic Taylor–Couette instability in Boger fluids, Rheol. Acta 34 (1995) 147.
[27] B.M. Baumert, S.J. Muller, Flow regimes in model viscoelastic fluid in a circular Couette system with independently rotating cylinders, Phys. Fluids 9 (1997) 566.
[28] Y.L. Joo, E.S.G. Shaqfeh, The effects of inertia on the viscoelastic Dean and Taylor–Couette flow instabilities with application to coating flows, Phys. Fluids A 4 (11) (1992) 2415.
[29] Y.L. Joo, E.S.G. Shaqfeh, Observations of purely elastic instabilities in the Taylor–Dean flow of a Boger fluid, J. Fluid Mech. 262 (1994) 27.
[30] D.W. Beard, M.H. Davies, K. Walters, The stability of elastico-viscous flow between rotating cylinders. Part 3. Overstability in viscous and Maxwell fluids, J. Fluid Mech. 24 (1966) 321.
[31] M. Avgousti, A.N. Beris, Viscoelastic Taylor–Couette flow: bifurcation analysis in the presence of symmetries, Proc. R. Soc. Lond. A 443 (1993) 17.
[32] M. Golubitsky, D.G. Schaeffer, I.N. Stewart, Singularities and Groups in Bifurcation Theory, vol. 2, Springer-Verlag, New York, 1998.
[33] P.J. Northey, R.C. Armstrong, R.A. Brown, Finite-amplitude time-periodic states in viscoelastic Taylor–Couette flow described by the UCM model, J. Non-Newtonian Fluid Mech. 42 (1992) 117.
[34] M. Avgousti, B. Liu, A.N. Beris, Spectral methods for the viscoelastic time-dependent flow equations with applications with Taylor–Couette flow, Int. J. Numer. Methods Fluids 17 (1993) 49.
[35] R. Kupferman, Simulation of viscoelastic fluids: Couette–Taylor Flow, J. Comp. Phys. 147 (1998) 22.
[36] M. Avgousti, A.N. Beris, Non-axisymmetric modes in the viscoelastic Taylor–Couette flow, J. Non-Newtonian Fluid Mech. 50 (1993) 225.
[37] M. Renardy, Y. Renardy, R. Sureshkumar, A.N. Beris, Hopf-Hopf and steady-Hopf mode interactions in the Taylor–Couette flow of an upper convected Maxwell liquid, J. Non-Newtonian Fluid Mech. 63 (1996) 1.
[38] R. Sureshkumar, A.N. Beris, M. Avgousti, Non-axisymmetric subcritical bifurcations in viscoelastic Taylor–Couette flow, Proc. R. Soc. Lond. A 447 (1994) 135.
[39] U.A. Al-Mubaiyedh, R. Sureshkumar, B. Khomami, Influence of energetics on the stability of viscoelastic Taylor–Couette flow, Phys. Fluids 11 (1999) 3217.
[40] U.A. Al-Mubaiyedh, R. Sureshkumar, B. Khomami, Linear stability of viscoelastic Taylor-Couette flow: influence of fluid rheology and energetics, J. Rheol. 44 (2000) 1121.
[41] U.A. Al-Mubaiyedh, R. Sureshkumar, B. Khomami, Nonlinear stability analysis of viscoelastic Taylor–Couette flow in the presence of viscous heating, Phys. Fluids 14 (2002) 1056.
[42] D.G. Thomas, R. Sureshkumar, B. Khomami, Effect of inertia on thermoelastic flow instability, J. Non-Newtonian Fluid Mech. 120 (2004) 93.
[43] J.M. White, S.J. Muller, Viscous heating and the stability of Newtonian and viscoelastic Taylor–Couette flows, Phys. Rev. Lett. 84 (2000) 5130.
[44] J.M. White, S.J. Muller, Experimental studies on the effect of viscous heating on the hydrodynamic stability of viscoelastic Taylor–Couette flow, J. Rheol. 47 (6) (2003) 1467.
[45] A. Groisman, V. Steinberg, Couette–Taylor flow in a dilute polymer solution, Phys. Rev. Lett. 77 (1996) 1480.
[46] B.J.A. Zeilinska, D. Mukamel, V. Steinberg, Multicriticality in viscoelastic fluids heated from below, Phys. Rev. A 33 (1986) 1454.
[47] A. Groisman, V. Steinberg, Solitary vortex pairs in viscoelastic Couette flow, Phys. Rev. Lett. 78 (1997) 1460.
[48] V. Steinberg, A. Groisman, Elastic versus inertial instability in Couette–Taylor flow of a polymer solution: review, Phils. Mag. B 78 (2) (1998) 253.
[49] A. Groisman, V. Steinberg, Mechanism of elastic instability in Couette flow of polymer solutions: experiment, Phys. Fluids 10 (1998) 2451.

[50] K.A. Kumar, M.D. Graham, Finite-amplitude solitary states in viscoelastic shear flow: computation and mechanism, J. Fluid. Mech. 443 (2001) 301.

[51] K.A. Kumar, M.D. Graham, Solitary coherent structures in viscoelastic shear flow: computation and mechanism, Phys. Rev. Lett. 85 (2000) 4056.

[52] R.G. Owens, T.N. Philips, Computational Rheology, Imperial College Press, 2002.

[53] R. Sureshkumar, A.N. Beris, Effect of artificial stress diffusivity on the stability of numerical calculations and the flow dynamics of time-dependent viscoelastic flows, J. Non-Newtonian Fluid Mech. 60 (1995) 53.

[54] R. Fattal, R. Kupferman, Constitutive laws for the matrix–logarithm of the conformation tensor, J. Non-Newtonian Fluid Mech. 123 (2004) 281.

[55] R. Fattal, R. Kupferman, Time-dependent simulation of viscoelastic flows at high Weissenberg number using the log-conformation representation, J. Non-Newtonian Fluid Mech. 126 (2005) 23.

[56] M.A. Hulsen, R. Fattal, R. Kupferman, Flow of viscoelastic fluids past a cylinder at high Weissenberg number: stabilized simulations using matrix logarithms, J. Non-Newtonian Fluid Mech. 127 (2005) 27.

[57] T.N. Phillips, I.M. Soliman, Influence Matrix Technique for the Numerical Spectral Simulation of Viscous incompressible Flows, Numer. Methods Partial Differential Eq. (1), John Wiley & Sons Inc., 1991, pp. 9–24.

[58] C. Canuto, M.Y. Houssaini, A. Quarteroni, T.A. Zang, Spectral Methods in Fluid Dynamics, Springer-Verlag, New York, 1988.

[59] L. Kleiser, U. Schumann, Treatment of incompressibility and boundary conditions in 3D numerical spectral simulations of plane channel flows, in: Proceedings of the Third GAMM Conference on Numerical Methods Fluid Mechanism, 1980, p. 165.

[60] U.A. Al-Mubaiyedh, R. Sureshkumar, B. Khomami, Effect of viscous heating on the stability of Taylor–Couette flow, J. Fluid Mech. 462 (2002) 111.

[61] R.J. Donnelly, N.J. Simon, An empirical torque relation for supercritical flow between rotating cylinders, J. Fluid Mech. 7 (1960) 401.

[62] A.N. Beris, R. Sureshkumar, Simulation of time-dependent viscoelastic channel Poiseuille flow at high Reynolds numbers, Chem. Eng. Sci. 51 (9) (1996) 1451.

[63] R. Sureshkumar, Numerical observations on the continuous spectrum of the linearized viscoelastic operator in shear dominated complex flows, J. Non-Newtonian Fluid Mech. 94 (2000) 205.